APPLICATION OF CROSSED-PLANE TOMOGRAPHY AND STEREO PARTICLE IMAGE VELOCIMETRY FOR THREE-DIMENSIONAL ANALYSIS OF PREMIXED TURBULENT FLAMES

A Dissertation

Presented to the Faculty of the Graduate School

of Cornell University

In Partial Fulfillment of the Requirements for the Degree of

Doctor of Philosophy

by

Sandra Sheila Sattler

May 2008

APPLICATION OF CROSSED-PLANE TOMOGRAPHY AND STEREO PARTICLE IMAGE VELOCIMETRY FOR THREE-DIMENSIONAL ANALYSIS OF PREMIXED TURBULENT FLAMES

Sandra Sheila Sattler, Ph. D.

Cornell University 2008

Crossed-Plane Laser Tomography (CPLT) and similar laser imaging methods have been used to measure instantaneous flamelet surface normal vectors in premixed turbulent flames to study the wrinkling of flamelet surfaces and the internal structure of the flamelet. CPLT was applied to measure flamelet orientations of premixed turbulent V-flames with increasing downstream distance from the stabilizing rod. Also, a combined CPLT and Stereo Particle Image Velocimetry (SPIV) technique was developed to measure flamelet orientation statistics, three dimensional reactant velocities, and flamelet displacement speeds in a turbulent V-flame. This technique was also used to measure in-plane flamelet curvature in laboratory V-flames. The distribution of flamelet orientations is found to have a simple universal form depending on a single parameter, ζ, for all flames studied to date. ζ and A_T/A, the mean flamelet area increase due to turbulence, grow linearly with distance from the stabilizer. The observed growth rates in ζ and A_T/A vary considerably from flame condition to flame condition, and the differences cannot be explained solely by changes in u'/S_L^o, the ratio of the turbulence intensity to the unstretched laminar flame speed.

Combined CPLT and SPIV are applied to measure three-dimensional flamelet orientation, reactant velocity, and flamelet displacement data in premixed turbulent

flames. Three-dimensional flamelet orientation information is calculated from two simultaneous, orthogonal imaging measurements. Using SPIV, three-dimensional seed particle velocity measurements are obtained using two cameras. Each camera records an image pair separated by a short time interval and views the same region of the flame from a different perspective. Based on these different views of particle displacements corrected for thermophoretic effects, all three components of reactant velocity are found. The combined CPLT and SPIV technique measured instantaneous, three-dimensional flamelet orientation, flamelet surface curvature and the flamelet displacement speed, defined as the component of the relative velocity between the reactants and the flame surface that is normal to the surface. Displacement speed data showed both a broad distribution of values and a significant probability of negative values. The breadth of the distribution and the presence of negative displacement speeds are attributed to high values of curvature and extensive tangential strain.

BIOGRAPHICAL SKETCH

The author was born on September 8, 1976 in Oakland, California. She spent most of her childhood in Oak Harbor, Washington where she graduated high school in the spring of 1994. The author attended Whitman College in the fall of 1994 and enrolled in the 3-2 engineering program with the School for Engineering and Applied Sciences at Columbia University. The author transferred to Columbia in 1996 and graduated from both Whitman College with a B.A. in Mathematics-Physics and from Columbia University with a B.S. in Mechanical Engineering in the spring of 1999. The author began graduate work at the Sibley School of Mechanical Engineering in the fall of 1999. The author left Cornell to work as an engineering consultant at TIAX LLC in Cambridge, MA in 2004. She defended her Ph.D. dissertation in the fall of 2007.

Dedicated to my mother, Remedios Sablan Sattler

ACKNOWLEDGMENTS

I would like to thank Professor F.C. Gouldin for giving me the opportunity to conduct this research, for serving as my advisor, and for providing me with the guidance to complete this work. I would also like to thank Professors E.M. Fisher and C.F. Pollock for serving on my special committee and for the advice they have provided throughout the research presented here. I would also like to thank many of my fellow graduate students for their assistance throughout this work, including Darin Knaus, Mike Feng, Mark MacDonald, Tina Jayaweera, Jennifer Edwards, Neil Boertlein, and Ryan Beresky. I would like to recognize Rick Schmidt for his technical assistance and Karen Biesecker and Marcia Sawyer for their administrative assistance. This work was supported with funding provided by the Army Research Office under several grants.

TABLE OF CONTENTS

LIST OF FIGURES

LIST OF TABLES

LIST OF SYMBOLS

A_T/A	Mean flamelet area increase due to turbulence
bw	The width of the histogram bin
B_T	Burning rate integral
c	Scalar reaction progress variable
<c>	Mean reaction progress variable
d	Flamelet displacement perpendicular to itself over time Δt
d_p	Seed particle diameter
$d\Omega(\theta,\varphi)$	Differential solid angle, defined as $\sin\varphi d\varphi d\theta$
F_{AT}	Particle inertial force
F_{SD}	Stokes drag force
F_{TP}	Thermophoretic force
I_o	Stretch factor that accounts for changes in the flamelet reaction rate due to turbulence
Ka	Karlovitz number
Kn	Knudsen number
m_p	Mass of seed particle
M	Mesh spacing
Ma	Markstein number
n_c	Average number of flamelet crossings per unit length of η
$\underline{n}_\eta$	unit vector aligned with η
N	Total number of samples in a distribution

$\underline{N}$	Flamelet surface normal vector
N_{bin}	Total number of data points in a specific histogram bin
$\underline{N}_L$	Unit vector in a plane containing the measurement line, pointed in the direction of laser propagation
$\underline{N}_{xy}$	Projection of $\underline{N}$ onto a two-dimensional plane
$\underline{N}_{<c>}$	Unit vector oriented normal to <c> surfaces
P_{bin}	The value of the PDF at a specific histogram bin
P_i	Probability of data point being in a specific histogram bin
Re_M	Grid turbulence Reynolds number, defined as u'M/ν
R_g	Specific gas constant
S_L	Flamelet displacement speed observed in the laboratory frame
S_L^d	Flamelet displacement speed
S_L^o	Unstretched laminar flame speed
S_L^d*/S_L^o	Normalized, density-weighted flamelet displacement speed
t	Time
T	Fluid temperature
u	Non-dimensionalized particle velocity magnitude
u_f	Local fluid velocity magnitude
u_p	Seed particle velocity magnitude
u'	Turbulence intensity
U	Bulk flow velocity
$\underline{U}_r$	Reactant velocity at the flamelet surface
<w>	Local mean reaction rate

x	Position within the flamelet
α	Angle between $\underline{N}_{xy}$ and η
γ	Fit parameter of the distribution of two-dimensional flamelet orientations
γ_p	Droplet kinematic viscosity
Δt	Time between the tomography laser pulse and the first SPIV laser pulse
Δx	Flamelet displacement along the measurement line
ζ	Fit parameter of the distribution of flamelet orientations
η	Arbitrarily oriented line for flamelet crossing statistics – best to define as normal to <c> constant surfaces
θ	Azimuthal angle used to specify $\underline{N}$
κ_f	Fluid thermal conductivity
κ_p	Particle thermal conductivity
κ_{tr}	Translational component of fluid thermal conductivity
λ	Mean free path of gas molecules
μ	Fluid viscosity
ν	Non-dimensionalized fluid velocity magnitude
ν_f	Fluid kinematic viscosity
ρ	Product density
ρ_o	Reactant density
ρ_f	Fluid density
ρ_p	Seed particle density
ρ_r	Reactant density
Σ	Flamelet surface density

τ	Non-dimensionalized time
φ	Polar angle used to specify $\underline{N}$
φ_{equiv}	Equivalence ratio
χ	Non-dimensionalized distance
$< >_f$	Average along η

CHAPTER 1

INTRODUCTION

Challenges of Energy and Combustion

The problem of energy sufficiency and environmental quality is currently a worldwide issue with many ramifications: national security, global warming, and energy storage, production and price. While new technologies for energy production are being developed and utilized - such as wind, geothermal and solar - the vast majority of the world's energy is still provided by fossil fuel combustion. Furthermore, the United States government estimates that combustion of fossil fuels accounts for more than 85% of all energy consumed in the United States [1]. The burning of fossil fuels provides nearly two-thirds of the electricity consumed in the U.S. and nearly all of the nation's transportation fuels. Even with aggressive development and deployment of new renewable and nuclear technologies, it is likely that the nation's reliance on fossil fuels will increase over the next two decades [2].

Recently, the focus on energy utilization in the global economy has opened the field of research and development in the area of fossil fuel combustion [3]. There is an unresolved problem of rapidly increasing energy demands but decreasing availability of fossil fuels. There is also a growing awareness of the negative effects of pollution which has resulted in the development and application of various types of emission controls. Solutions are needed to reduce energy requirements by providing clean and efficient fossil fuel combustion to maintain a sustainable energy supply and to protect the environment. The development of advanced combustion technologies that are highly efficient and produce low emissions is an important priority for national security as well as for the economy and the environment [3]. This must be accomplished by improvements in current energy conversion technologies in

efficiency and advanced control to increase their productivity and reduce overall fuel consumption. Such developments could be achieved faster and cheaper if accurate, robust and truly predictive combustion models were available.

Importance of Premixed Turbulent Combustion

In most energy producing processes, combustion takes place in turbulent rather than laminar conditions. Turbulence increases mixing processes and thus enhances combustion. Also, combustion releases heat which causes flow instability by buoyancy and gas expansion, which enhances the transition to turbulence. There are several important practical applications of premixed turbulent combustion, such as spark-ignition engines, premixed prevaporized gas turbines, and industrial furnaces.

There are still many unresolved problems in understanding premixed turbulent combustion. Turbulence itself is far from being fully understood – it is agreed to be the most significant unresolved problem in classical physics [4]. The need to understand practical engineering problems has led to the development of non-reacting turbulent flow models. The current helpfulness of using these models in industry has encouraged similar approaches in the area of premixed turbulent combustion. Due to the complex nature of premixed turbulent combustion (the coupling of fluid dynamics with chemical reactions), realistic numerical models for premixed turbulent combustion are still being developed [4].

Currently, direct numerical simulation (DNS) of the coupled equations of fluid motion, molecular transport, and chemical reaction can only be applied to simple laboratory-scale turbulent flames [5-6]. These simulations for practical devices are prohibitively computationally expensive. In turbulent combustion, molecular mixing occurs on the smallest scale of turbulence, so even the smaller scales of the thin reaction layers need to be resolved. With the large difference in scales between the

thin reaction layers and the size of the combustion chamber, these simulations require hundreds of millions of computational cells and millions of processor hours [3]. To develop and analyze new practical combustion devices cheaply and quickly, simplified computational models are needed. The development and validation of new and improved simplified models need experimental data.

Here, laser diagnostics techniques (crossed-plane laser tomography and stereo particle image velocimetry) in laboratory-scale experiments are designed to study premixed turbulent combustion phenomena at a fundamental level. Laser diagnostic methods are desirable due to their non-intrusiveness, repeatability, and high spatial and temporal resolution. These techniques are also intended to provide insights and data to promote the development and validation of advanced combustion models.

The Flamelet Model

In premixed turbulent combustion the fuel and oxidizer are mixed well before they are burned in a turbulent flow environment. For a range of turbulence conditions chemical reactions and scalar quantitative variations can be assumed to be confined to thin sheets, what is known as the flamelet regime. For flames fitting these conditions, flamelet models have been developed by Bray, Moss, and Libby (BML) and others [7-11]. In these flamelet models, the location of the flame is defined by a thin wrinkled surface and the flame's structure is that of a stretched laminar flame. The reaction rate of a flame in the flamelet regime is related to the amount of flamelet surface area in a volume and the modification of the local laminar flame speed due to stretch and unsteadiness. The local mean reaction rate of the flame, $\langle w \rangle$, is thus proportional to the average flamelet surface area per unit volume, (the surface density Σ), and the mean reaction rate per unit flamelet surface area [12]. It is shown that a major effect of turbulence is to wrinkle the flamelet, increasing the surface density, Σ, and the local

mean reaction rate can be expressed as

$$\langle w \rangle = \rho_r S_L^o I_o \Sigma \,, \tag{1.1}$$

where ρ_r is the density of the reactants, S_L^o is the unstretched laminar flame speed, and I_o is a factor that accounts for changes in the flamelet reaction rate due to turbulence, i.e. the stretch factor [13]. The first two terms of Eq. 1.1 are easily found, it is the last two terms that are of great interest.

The BML model [8] introduces the scalar reaction progress variable c, where c describes the extent of chemical reaction and has the value of zero in reactants and one in products. The mean reaction progress variable, <c>, is ensemble-averaged and varies continuously from zero on the reactants side of the flame brush to one on the products side. For a planar turbulent flame, <c> constant surfaces are parallel planes.

Numerous model equations [eg.14-16] and DNS studies [eg. 17-18] have been performed to find Σ. Bray, Moss, and Libby [19] have used flamelet crossing statistics to develop an algebraic model to find Σ. Gouldin [20] has developed an expression for Σ in terms of flamelet crossings of an arbitrarily oriented line, η.

$$\Sigma = \left\langle \frac{1}{\left| \underline{N} \bullet \underline{n}_\eta \right|} \right\rangle_c n_c \tag{1.2}$$

where $\underline{N}$ is the flamelet surface normal vector, a unit vector oriented towards reactants, $\underline{n}_\eta$ is a unit vector aligned with η and n_c is the average number of flamelet crossings per unit length of η. The direction of η is arbitrary [20]; however for reasons discussed in Reference [21] it is best to define it to be normal to <*c*>, mean progress variable, constant surfaces. The *c* subscript indicates that the average is crossing-weighted. When performing a crossing weighted average, the contribution to the average associated with a given orientation $\underline{N}$ is weighted by the probability of a flamelet with that orientation crossing the reference line, *η*. A consequence of this weighting is that the singularity in Eq. (1.2) associated with $\underline{N}$ perpendicular to *η* is

eliminated [21].

Many workers have investigated experimentally the distribution of $\underline{N}$ required to evaluate Σ [18, 22-24]. Most of these studies are examples of two-dimensional imaging, such as those obtained from planar laser induced fluorescence (PLIF), laser tomography, or Rayleigh imaging. Only two-dimensional information on $\underline{N}$ can be found from these data. To extract three-dimensional information from laser tomography images assumptions need to be made about the out-of-image plane component.

At Cornell we have developed a dual plane imaging method, crossed-plane laser tomography, in order to measure $\underline{N}$ directly in three dimensions [21, 25-29]. The crossed-plane imaging technique used to find $\underline{N}$ involves simultaneous orthogonal, single plane imaging measurements. Two orthogonal laser sheets define the two orthogonal imaging planes. The laser sheets intersect along a line referred to as the measurement line. Where the flamelet crosses the measurement line, three-dimensional flamelet orientation data can be measured. Repeated measurements are made to build a set of $\underline{N}$ and crossing density, n_c, data.

With $\underline{N}$ specified in spherical coordinates by a polar angle, φ, and an azimuthal angle, θ, and the polar axis chosen to be normal to $<c>$ constant surfaces (i.e. aligned with η), the crossing-weighted probability density function (pdf) of $\underline{N}$ has been found to be

$$P_c(\theta,\varphi)d\Omega(\theta,\varphi) = C\left|\cos\varphi\right|\exp-(\varphi/\zeta)^2\sin\varphi d\varphi d\theta\,, \qquad (1.3)$$

where the line crossed is the polar axis and $d\Omega(\theta,\varphi)$ is the differential solid angle $\sin\varphi d\varphi d\theta$. According to Eq. (1.3) the pdf of $\underline{N}$ is independent of θ, quasi-Gaussian in φ, and depends on a single fit parameter ζ; C is a normalization constant [21].

This form for the crossing-weighted pdf of $\underline{N}$ leads to simple expressions for both Σ and the burning rate integral, B_T [7]. The burning rate integral is defined as the

path integral of the mean reaction rate, <w>, across the flame brush

$$B_T = \int_{-\infty}^{\infty} \langle w \rangle d\eta \tag{1.4}$$

where η again is a path normal to <c> surfaces. From Eq. 1.3, it is seen that Σ is a function of ζ and n_η alone. B_T is the line integral of $\langle w \rangle$ along η. By substitution of Eq. 1.2 into 1.1 and integrating one obtains $B_T = \rho_r S_L^o \langle I_o \langle |1/\underline{N} \bullet \underline{n}_\eta| \rangle_c \rangle_f n_c$ where $\langle \rangle_f$ denotes an average along η. Eq. 1.3 can also be used in this expression so that B_T becomes a function of $\zeta(\eta)$ and n_c. Since ζ and n_η can be measured, Σ and B_T can be calculated, where I_o is estimated based on *a priori* knowledge.

The crossed-plane imaging method was first demonstrated at Cornell by Bingham in his thesis [25], which is the first three-dimensional $\underline{N}$ data published. This method has since been applied to V-flames [26, 27] and engine flames [28, 29]. The results of these measurements suggest that the form of the probability density function (PDF), Eq. 1.3, of $\underline{N}$ is universal.

Thesis Organization

The simple universal form of the distribution of flamelet orientations $\underline{N}$ and its dependence on a single parameter, ζ, is demonstrated in the succeeding chapter. It is shown that ζ can be determined from two-dimensional image data provided that the image plane is aligned perpendicular to <c> constant surfaces. To further show the power of this technique, single plane measurements were made on seven methane-air, turbulent V-flames. ζ and A_T/A, the mean flamelet area increase due to turbulence, are found to grow linearly with distance from the V-flame stabilizing rod. The observed growth rates in ζ and A_T/A vary considerably from flame to flame, and the differences can not be explained solely by changes in u'/S_L^o, the ratio of the turbulent intensity to the unstretched laminar flame speed.

The third chapter is titled "The Combined Crossed-Plane Tomography and Stereo Particle Image Velocimetry Method." Here the combined crossed-plane laser tomography and stereo particle image velocimetry (SPIV) method is described in detail. Three-dimensional flamelet orientation information is calculated from two simultaneous, orthogonal imaging measurements. Using SPIV, three-dimensional reactant velocity measurements are obtained using two cameras. All three components of flamelet orientation, flamelet surface curvature and reactant velocity can be combined to find the flamelet displacement speed, which is defined here as the component of velocity relative and normal to the flame surface.

The fourth chapter discusses the thermophoretic force and the importance of its consideration in SPIV measurements. The accuracy of laser imaging techniques for measuring fluid velocities in seeded flows (such as laser-Doppler velocimetry and SPIV) depends on how closely the seeding particles follow the flow. The thermophoretic force is the force that a particle feels as it travels through regions of high temperature gradients. In these regions, the molecules on the hotter side of a seed particle have, on average, higher momenta than those on the cooler side of the seed particle, resulting in a net force on the particle in the direction of decreasing temperature. This chapter describes the formulation of the thermophoretic force correction for seeded flow in regions of high temperature gradients.

In the fifth chapter the combined crossed-plane laser tomography and stereo particle image velocimetry (SPIV) method is applied to a turbulent V-flame to measure three-dimensional flamelet orientation, reactant velocity, and flamelet displacement data in premixed turbulent flames. From these data, the velocity components of the seed particles perpendicular to the flamelet surface are determined and corrected for thermophoretic effects to find the reactant velocity. The flamelet displacement speed is obtained from the measurements of flamelet displacement and

reactant velocity at the flamelet surface. Displacement speed data show both a broad distribution of values and a significant probability of negative values. The breadth of the distribution and the presence of negative displacement speeds are attributed to high values of curvature and extensive tangential strain.

The sixth chapter analyzes the combined crossed-plane tomography method and discusses the calculated uncertainty in the flamelet displacement speed measurements. Measurements made with the combined crossed-plane tomography and stereo PIV method are subject to four types of errors: (1) Those due to instrumentation, i.e.: system setup and image processing, (2) those due to uncertainty in the calibration of the crossed-plane tomography measurement technique, (3) those due to uncertainty in the calibration of the SPIV measurement technique, and (4) those due to the seed particles not faithfully following the flow, i.e.: thermophoretic effects. The individual sources of error and how these errors propagate to the calculated uncertainty in the flamelet displacement speed are discussed in this chapter.

Also included in this dissertation is a general summary.

CHAPTER 2

TOMOGRAPHY AND FLAMELET NORMAL MEASUREMENTS

At Cornell we have developed a dual plane imaging method, crossed-plane laser tomography, in order to measure $\underline{N}$ directly in three dimensions. Laser tomography (described by Boyer [30]) allows for the visualization of an instantaneous picture of a flamelet surface in a planar cross section of a flame. The reactant flow is seeded with an aerosol of oil droplets that are consumed within the flamelet. The flame is illuminated with a laser beam that has been formed into a thin sheet. The droplets in the reactants Mie scatter laser light; no scattering occurs in products where there are no droplets. A camera is oriented normal to the laser sheet and an image of the light scattering is recorded. The image is an instantaneous visualization of the flamelet surface as the exposure time (either the laser pulse duration or the exposure time of the camera) is short compared to the characteristic time of flamelet motion. Within each image, the boundary between light reactants and dark products represents the intersection of the flamelet surface and the imaging plane, the flamelet curve. The flamelet curve represents the instantaneous flamelet location within the flame cross-section defined by the laser sheet.

Single plane laser tomography yields flamelet surface geometry information only within the laser scattering plane. The crossed-plane laser tomography technique measures the instantaneous three-dimensional flamelet surface normal, $\underline{N}$, and involves simultaneous orthogonal, single plane imaging measurements. Two orthogonal laser sheets define the two orthogonal imaging planes. The laser sheets intersect along a line referred to as the measurement line. Where the flamelet crosses the measurement line within each of the two images, vectors tangent to the flamelet curve are measured. The cross-product of the two tangent vectors yields the three-

dimensional flamelet surface normal, $\underline{N}$. Repeated measurements are made to build a set of $\underline{N}$ and crossing density, n_c, data. An example of the crossed-plane laser tomography measurement method and a schematic of the orthogonal imaging planes are shown in Fig. 2.1. Here crossed-plane laser tomography is applied to a perturbed laminar V-flame.

Determination of Three-Dimensional Flamelet Orientation Distributions in Turbulent V-Flames from Two-Dimensional Image Data

The crossed-plane imaging technique used to find $\underline{N}$ [18, 21, 26, 27] involves simultaneous orthogonal, single plane imaging measurements; three-dimensional flamelet orientation data are obtained only along the line of intersection of the two laser sheets. It is desirable to be able to extract three-dimensional $\underline{N}$ data from single plane, two-dimensional image measurements given the large amount of existing single-plane image data and the simplicity of such measurements. Also a single plane technique allows measurements of flamelet orientation in any region of the image plane.

Several workers have performed two-dimensional imaging measurements to determine the distribution of $\underline{N}$ to evaluate Eq. 1.2. To extract three-dimensional information from laser tomography images Shepherd and Ashurst [18] made arguments based on symmetry and assumed a lack of correlation between in plane (the image plane) and out of plane components of $\underline{N}$ in a stagnation point flame. Alternately, Lee et al [22, 23] used planar laser induced fluorescence (PLIF) to study flamelet curvature and assumed that out of image plane curvature is approximately the same as in plane.

Given the nature of the form of the distribution of $\underline{N}$ in Eq. 1.3, it is possible to

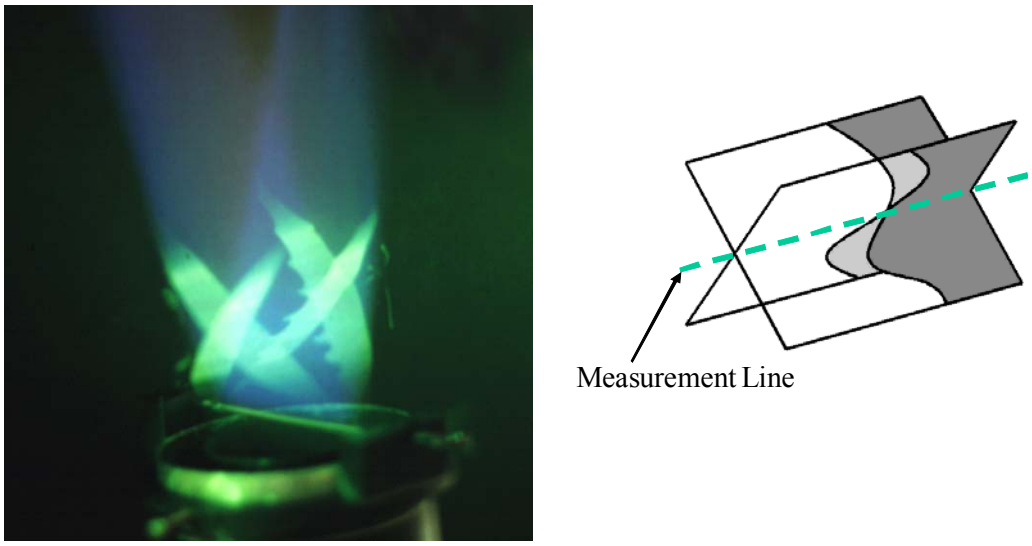

Figure 2.1: Photograph of the crossed-plane laser tomography technique used on a perturbed laminar V-flame. Laser light is Mie scattered off of an aerosol of oil droplets seeded into the reactants. Also shown is a schematic representation of the two orthogonal tomography imaging planes. The line of intersection of the two planes is the measurement line, where flamelet orientation and crossing data is recorded.

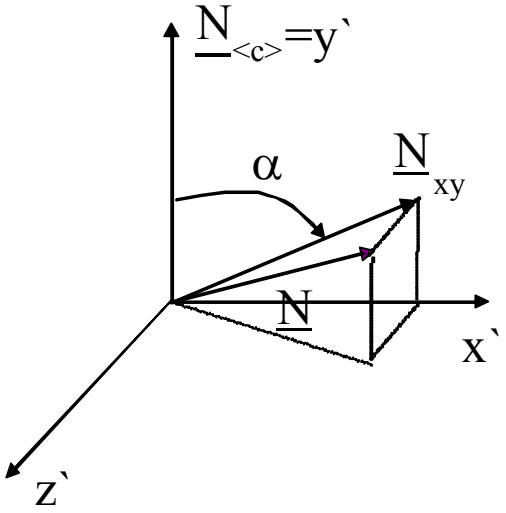

Figure 2.2: The coordinate system used for single-plane imaging measurements. One laser sheet is within the x'y' plane. The coordinate system is defined such that y' is oriented perpendicular to <c>=constant surfaces. $\underline{N}_{xy}$ is the three-dimensional flamelet surface normal $\underline{N}$ projected onto the x'y' plane.

determine three-dimensional orientation information from two-dimensional image data. The relationship between the pdf of the projection of $\underline{N}$ onto a two-dimensional plane, $\underline{N}_{xy}$, (for a special orientation of x and y, see Fig. 2.2) and that of $\underline{N}$ as given in Eq. (1.3) is developed here.

It is found that because of symmetry in the azimuthal direction, three-dimensional information can be extracted from two-dimensional image data if the imaging plane contains the polar axis. $P_c(\alpha)$, the crossing-weighted PDF of the angle, α, between $\underline{N}_{xy}$ and η that is defined over the interval –180 to + 180 degrees, is generated from the crossing-weighted PDF of $\underline{N}$ through Monte-Carlo computations. The resulting PDF is found to depend on a single fit parameter, γ. In addition, it is found to be symmetric about $\alpha = 0$, and consequently in the results reported α is replaced by its magnitude. A plot of γ versus ζ is obtained by computation and fit to a polynomial giving a simple relationship between the two parameters.

The evolution of the ζ fit parameter with increasing downstream distance in 7 different methane-air V-flames is studied to demonstrate the utility of the relationship developed between the PDFs. $\underline{N}_{xy}$ is measured by imaging Mie scattering from a single, vertical plane perpendicular to the V-flame stabilizing rod. From each recorded image data for α are collected along six different η lines that are locally perpendicular to $\langle c \rangle$ constant lines. The location of each line is defined by the axial location where it crosses the $\langle c \rangle = 0.5$ line. The PDF of α and the two-dimensional fit parameter γ are obtained from repeated measurements. ζ is determined from each measured γ using the above relationship between γ and ζ.

A Monte- Carlo numerical procedure is used to establish the relationship between $P_c(\theta,\varphi)$, and $P_c(\alpha)$. To do this, the universal form of the PDF of $\underline{N}$, Eq. (1.3) is assumed to be valid. A simple relationship between a given orientation $\underline{N}(\varphi,\theta)$ and its projection onto the x-y plane $\underline{N}_{xy}(\alpha)$ exists;

$$\alpha = \tan^{-1}\left(\tan\phi\cos\theta\right). \qquad (2.1)$$

For a large set of *n* flamelet normal vectors, {N}, distributed according to Eq. (1.3), the number of vectors in a differential solid angle dΩ that cross η is

$nC|\cos\varphi|\exp-(\varphi/\zeta)^2 d\Omega$. This relationship is used to generate $P_c(\alpha)$. For each dΩ(φ,θ) a histogram of α is incremented by the fraction of *n* in dΩ(φ,θ) with a projection in the α value range corresponding to that particular dΩ(φ,θ) Then the histogram is normalized and fit to a smooth curve to obtain an estimate of $P_c(\alpha)$.

It should be noted that the flamelet polar angle is limited to a maximum value of 180°. Previous experiments [26-28] measured relatively low values of ζ, so that the probability of finding φ ~180° was negligible. To determine the relationship between the PDFs of α and of φ and θ a wide range of ζ values is used and at high ζ the probability of φ~180° is not negligible. Consequently, for large values of ζ, (and of γ), the exponential term in Eq. 1.3 is clipped at φ = 180°. While clipping seems reasonable, we do not have experimental data at high turbulence levels to confirm its validity.

The Monte-Carlo procedure is applied for 20 evenly spaced values of ζ between 10° and 100° and 64800 equal size segments of 4π steradians; ΔΩ (φ,θ)=4π/64800 steradians. The resulting α PDF is found to be fit well by

$$P_c(\alpha) = C'|\cos\alpha|\exp-(\alpha/\gamma)^2, \qquad (2.2)$$

a form similar to that of Eq. 1.3 with a single fit parameter γ. The *c* subscript indicates the distribution is crossing weighted. γ values generated over the range of ζ values are plotted in Fig. 2.3 where it is seen that γ ~ ζ for small ζ but deviates from the linear relationship for larger ζ. This relationship between the two and three dimensional distributions and fit parameters is exploited in the following section to find ζ from single plane data.

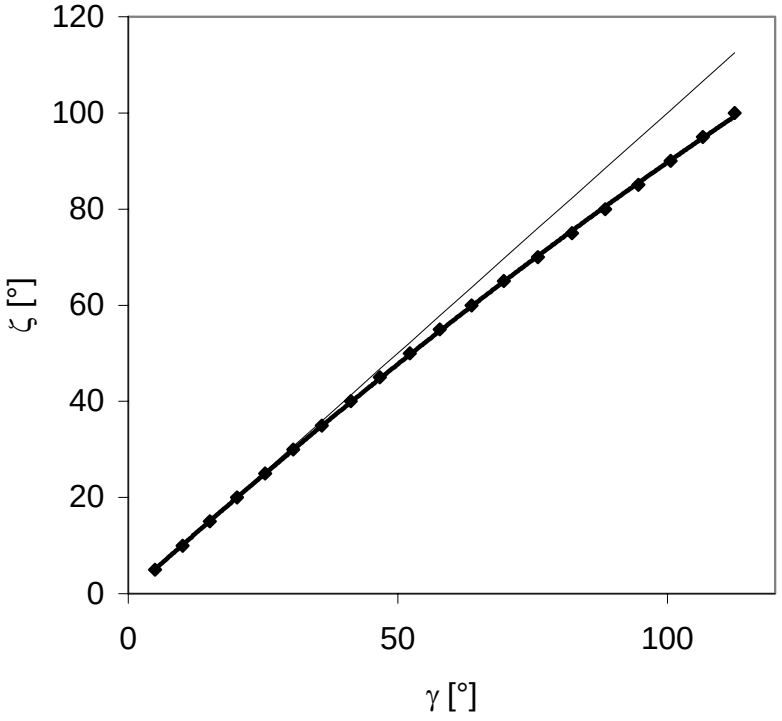

Figure 2.3. γ, the PDF fit parameter of $\underline{N}_{xy}$, generated over a range of ζ, the PDF fit parameter of $\underline{N}$. The data are fit by $\zeta=-0.0011\gamma^2+1.0097\gamma+0.0954$.
The $\zeta=\gamma$ line is plotted to demonstrate that $\gamma\sim\zeta$ for small ζ but deviates for larger ζ.

Description of Apparatus

Single plane laser tomography measurements were performed on the V-flame burner used in several previous studies in this laboratory [25-27, 31-32]. Two of these studies have shown that the form of the PDF of $\underline{N}$ in Eq. 1.3 is applicable to turbulent V-flames [26-27]. $\langle c \rangle$ surfaces contain the stabilizing rod of the V-flames, and to take advantage of the above results, the imaging plane is aligned perpendicular to the stabilizing rod so as to contain normals to $\langle c \rangle$ constant surfaces. A frequency doubled Nd:YAG pulsed laser is used for tomographic visualization. The beam is formed into a thin sheet defining the imaging plane (Fig. 2.4).

The reactants are seeded with micron sized silicone oil droplets which are consumed within the flamelet such that Mie scattering of laser light occurs in the reactants but not the products. Tomographic images are recorded with an ICCD camera having a 512 x 512 pixel CCD array. The field of view imaged is 40 mm x 40 mm with an exposure time of 20 ns; the camera spatial resolution is better than 0.2 mm. A polarizing filter is used to block background light. The timing sequence for the camera is initiated by a trigger pulse from the laser.

Fuel and air flow rates measured with mass flow meters are used to determine the bulk flow velocity, U, and the equivalence ratio φ_{equiv}. To reduce interference from light scattered by room air dust, the premixed flame is sheathed by a co-axial flow having a velocity similar to the reactant flow. Turbulence is generated by two different wire mesh grids positioned 50 mm upstream from the stabilizing rod. The first grid has approximately 4.5 squares/cm^2, a 0.86 mm wire diameter and a mesh spacing, M, of 4.2 mm; the second grid has approximately 1.7 squares/cm^2, a 1.59 mm x 1.59 bar, and M=6 mm. u', the turbulence intensity, was measured for a fixed value of the bulk velocity, U, at various downstream distances using hot wire anemometry, and the ratio u'/U is fit as a function of distance. This function is then used to find u'

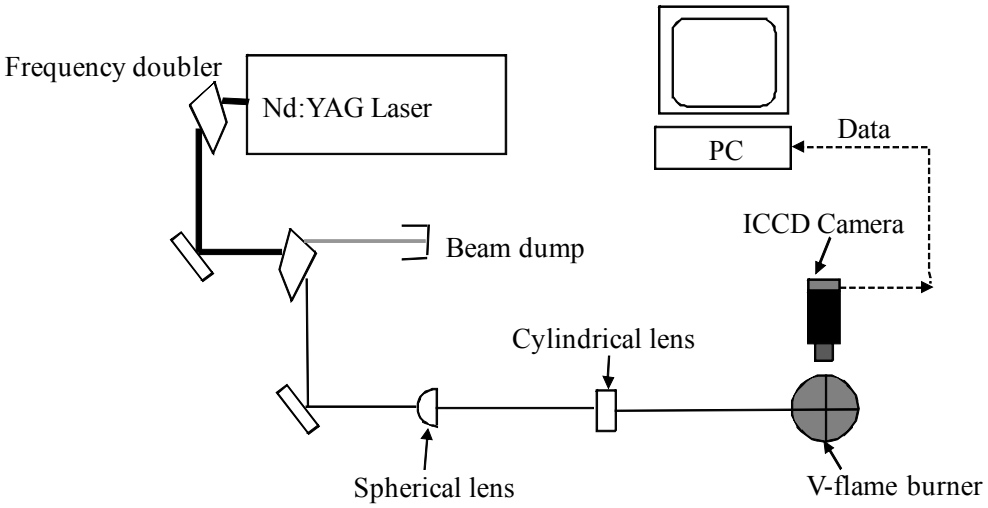

Figure 2.4: Schematic diagram of single-plane laser tomography experimental setup. A single beam is formed into a thin sheet in a vertical plane over the V-flame burner. Imaging data are collected by an ICCD camera and are stored for post-processing on a PC.

for the bulk flow velocities used in this study.

Tomographic images were recorded and saved for post processing. The recorded images are bright in the reactants due to Mie scattering and are dark in the products, Fig. 2.5. The boundary between light and dark regions represents the intersection of the flamelet surface and the imaging plane, the flamelet curve. Image processing consists of a thresholding step, making the images binary, followed by a spatial averaging step to remove noise of scales smaller than the 0.2 mm camera resolution [33]. The flamelet curve is fit locally to a smooth curve to find its normal. Further details on image processing can be found in [25].

The $\langle c \rangle$ field is required to determine $\underline{N}_{\langle c \rangle}$, the orientation of $\underline{\eta}$. The instantaneous c field is generated for each processed laser tomography image by assigning a c value of 0 to reactant pixels and of 1 to product pixels. The c fields from all images are averaged, yielding the $\langle c \rangle$ field, and the $\langle c \rangle$=0.5 contour is used to define $\underline{N}_{\langle c \rangle}$. $\underline{N}_{xy}$ measurements were made at six η lines, beginning at 30 mm above the stabilizing rod and incrementing in 5 mm steps; except for flame 7 which had increments of 10 mm. The η paths are shown in Fig. 2.5.

Flamelet crossings are identified at points where the flamelet curve intersects η. Polynomial curves are fit along the flamelet curve in regions adjacent to crossings, and the slope of the fit at the crossing is used to determine $\underline{N}_{xy}$. α, the magnitude of the angle between $\underline{N}_{xy}$ and η, is obtained from the slope. At each downstream measurement location a histogram of α values is generated and subsequent normalization gives its PDF, $P_c(\alpha)$.

Results and Discussion

Single plane measurements were performed on seven different methane-air V-flames with three different equivalence ratios, three different mean velocities and two

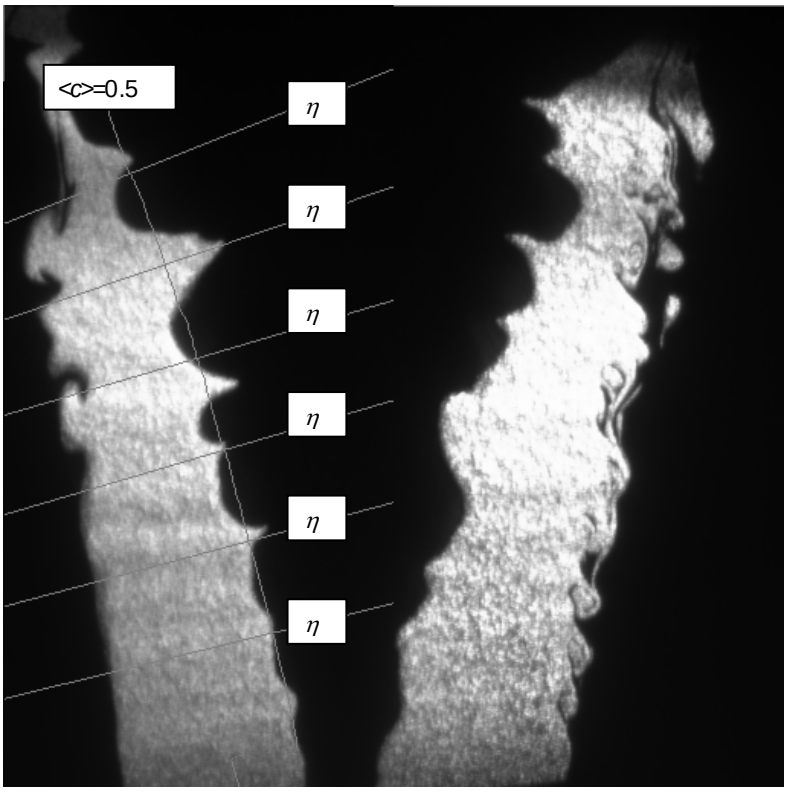

Figure 2.5: Sample image of flame 7. The image is bright in the reactants where laser photons Mie scatter off of the silicone oil droplets and are dark in products. $<c>=0.5$ is used to define $\underline{N}_{<c>}$. η, the reference line for measuring α, is aligned with $\underline{N}_{<c>}$. η paths for the six downstream distances studied are shown, spaced 10 mm apart. Flamelet crossings are identified at points where the flamelet curve intersects the different η paths. The flamelet curve at the crossing is fit locally to a smooth curve, its slope is used to determine $\underline{N}_{xy}$.

different turbulence-generating grids. The flame conditions and results are summarized in Table 2.1. Between 600 and 2000 vertical images were analyzed for each flame. From each recorded image data for α and N_c, the average number of times the flamelet crosses an η line, were obtained for each of the η lines.

From the angle data**,** PDFs were estimated and fit to a function of the expected form in order to find γ. Sample results are shown in Figure 2.6, where it can be seen that the agreement between the data and fit is quite good. The γ values obtained from these fits are used to find ζ, and the results are shown in Table 2.1 as well as in Figure 2.7 as plots of ζ versus downstream distance from the flame stabilizing rod, x, scaled by M. These plots show that the level of flamelet wrinkling increases with distance, and that the increase as measured by ζ is approximately linear over the region of measurement. It is noted that for flame 2, ζ values at only four locations are reported. This is because in this flame, at large x values, the flamelet approached the boundary between the premixed and co- flows, and it was not possible for the image analysis algorithm to distinguish between the flamelet curve and the boundary curve separating the two flows.

Because the flame is anchored by a rod and wrinkling is therefore suppressed near the rod, we expect ζ to tend to zero as x goes to zero. Extrapolations of the lines in Figure 2.7 to $x = 0$ imply that the behavior of ζ near the rod is nonlinear. Furthermore, it is likely that this behavior depends on the rod wake as well as the flow turbulence properties. The downstream behavior of ζ versus x/M is unknown. In the present case, image data show that after approximately 80 mm downstream wrinkling is effected by the annular air co-flow.

Eq. 1.3 can be integrated along ζ lines to obtain an expression for the mean flamelet surface area per unit flame brush area, A_T/A; this is the area ratio term first

Table 2.1: Summary of flame conditions and measurement results. Note that the turbulence conditions listed for flame 7 were measured at the location of the stabilizer rod. Re_M is the Reynolds number for grid turbulence, defined as $u'M/\nu_f$ where ν_f is the kinematic viscosity of the reactants. Re_M is comparable in magnitude to the turbulence Reynolds number based on the integral scale of the reactant flow.

Flame	x [mm]	V-flame 1/2 angle [°]	U [m/s]	u' [m/s]	Φ	S_L [m/s]	grid	u'/S_L	Average of u'/S_L	Re_M	γ [°]	ζ [°]	N_c
1	30	18	2	0.11	0.65	0.16	1	0.701	0.600	26.6	25.6	25.2	1
	35	18	2	0.10	0.65	0.16	1	0.656		24.9	29.8	29.2	1
	40	18	2	0.09	0.65	0.16	1	0.615		23.3	35.1	34.2	1
	45	18	2	0.09	0.65	0.16	1	0.576		21.8	42.5	41.0	1.003
	50	18	2	0.08	0.65	0.16	1	0.541		20.5	50.1	47.9	1.014
	55	18	2	0.08	0.65	0.16	1	0.510		19.3	58.7	55.6	1.026
2	30	19	2	0.25	0.65	0.16	2	1.662	1.5013	90.0	48.6	46.6	1.045
	35	19	2	0.23	0.65	0.16	2	1.544		83.6	55.5	52.7	1.044
	40	19	2	0.22	0.65	0.16	2	1.442		78.1	65.4	61.4	1.102
	45	19	2	0.20	0.65	0.16	2	1.357		73.5	71.4	66.6	1.086
3	30	11	4	0.19	0.65	0.16	1	1.292	1.172	49.0	30.2	29.6	1
	35	11	4	0.19	0.65	0.16	1	1.235		46.8	32	31.3	1
	40	11	4	0.18	0.65	0.16	1	1.185		44.9	37.5	36.4	1
	45	11	4	0.17	0.65	0.16	1	1.142		43.3	40.6	39.3	1.001
	50	11	4	0.17	0.65	0.16	1	1.105		41.9	44.9	43.2	1.010
	55	11	4	0.16	0.65	0.16	1	1.075		40.8	49.6	47.5	1.023
4	30	15	4	0.49	0.65	0.16	2	3.243	2.689	175.6	46.9	45.0	1.005
	35	15	4	0.45	0.65	0.16	2	2.982		161.5	47.6	45.7	1.006
	40	15	4	0.41	0.65	0.16	2	2.750		148.9	54.1	51.5	1.012
	45	15	4	0.38	0.65	0.16	2	2.548		138.0	55.8	53.0	1.018
	50	15	4	0.36	0.65	0.16	2	2.377		128.7	70	65.4	1.033
	55	15	4	0.34	0.65	0.16	2	2.235		121.0	77.2	71.5	1.048
5	30	18	4	0.19	0.8	0.28	1	0.692	0.6282	49.0	48.7	46.7	1.009
	35	18	4	0.19	0.8	0.28	1	0.662		46.8	55.8	53.0	1.017
	40	18	4	0.18	0.8	0.28	1	0.635		44.9	62.9	59.3	1.028
	45	18	4	0.17	0.8	0.28	1	0.612		43.3	75.4	70.0	1.055
	50	18	4	0.17	0.8	0.28	1	0.592		41.9	82.1	75.6	1.074
	55	18	4	0.16	0.8	0.28	1	0.576		40.8	86	78.8	1.106
6	30	18	4	0.49	0.8	0.28	2	1.738	1.441	175.6	59.8	56.5	1.023
	35	18	4	0.45	0.8	0.28	2	1.597		161.5	69.8	65.2	1.042
	40	18	4	0.41	0.8	0.28	2	1.473		148.9	77.6	71.8	1.046
	45	18	4	0.38	0.8	0.28	2	1.365		138.0	82.9	76.2	1.109
	50	18	4	0.36	0.8	0.28	2	1.273		128.7	93.6	85.0	1.143
	55	18	4	0.34	0.8	0.28	2	1.197		121.0	90.4	82.4	1.158
7	30	14	2.61	0.12	0.7	0.21	1		0.57	30.3	21.9	21.7	1
	40	14	2.61		0.7	0.21	1				33	32.2	1
	50	14	2.61		0.7	0.21	1				38.9	37.7	1.003
	60	14	2.61		0.7	0.21	1				53.8	51.2	1.003
	70	14	2.61		0.7	0.21	1				65	61.1	1.003
	80	14	2.61		0.7	0.21	1				65.6	61.6	1.037

proposed by Damkohler to account for the increase in burning rate due to turbulence in the flamelet regime.

$$A_T/A = \left\langle \left\langle 1/\left|\underline{N} \bullet \underline{n}_\eta\right| \right\rangle_c \right\rangle_f N_c \quad , \tag{2.3}$$

N_c is the line integral of n_η and has been measured, Table 2.1. As would be expected N_c increases with distance from the rod but not linearly. In Reference [21] it is shown that for flamelet normals distributed according to Eq. 1.3 the direction cosine term is a nearly monotonic but nonlinear function of ζ varying from 1 to 2. This relationship has been used to find $\langle\langle 1/|\underline{N}\bullet\underline{n}_\eta|\rangle_c\rangle_f$ and hence A_T/A. The results are presented in Fig. 2.8, where it is seen that A_T/A increases linearly with distance for the region of observation. Since as noted, wrinkling is suppressed by the stabilizer rod, one expects A_T/A to go to 1 near the rod. In turn, both N_c and the direction cosine term are expected to go to one.

The results for ζ, N_c and A_T/A show that these quantities increase with distance from the stabilizer rod and that for ζ and A_T/A the increase is linear. There are considerable differences in growth rate between the different flames. Burning velocity is widely considered to be a function of u'/S^o_L, and Gülder has suggested several correlations for burning velocity having u'/S^o_L as well as the turbulence Reynolds number as independent variables [34]. Based on this experience it seems reasonable to expect the slopes of the ζ versus x/M lines, the growth rates, to depend on u'/S^o_L and perhaps Reynolds number. In Figure 2.9 growth rates are plotted against an average u'/S^o_L for each flame studied. The vertical error flags are estimated uncertainties in finding the slopes of the lines in Figure 2.7, while the horizontal bars

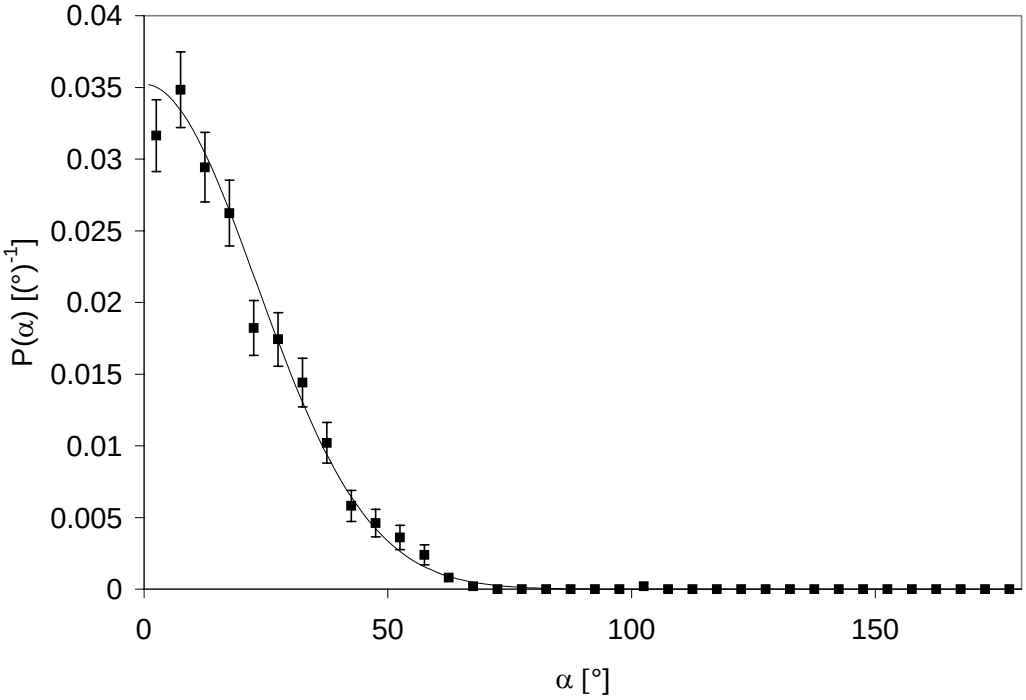

Figure 2.6: Sample PDF of measured $\underline{N}_{yz}$ in α for x=40 mm for flame 7. The data are fit to the form $P_c(\alpha)=C'|\cos\alpha|\exp-(\alpha/\gamma)^2$ using a least squares fit. γ=33° and the uncertainty, χ^2, is 0.0001. The error bars shown indicate error due to statistical uncertainty in the data.

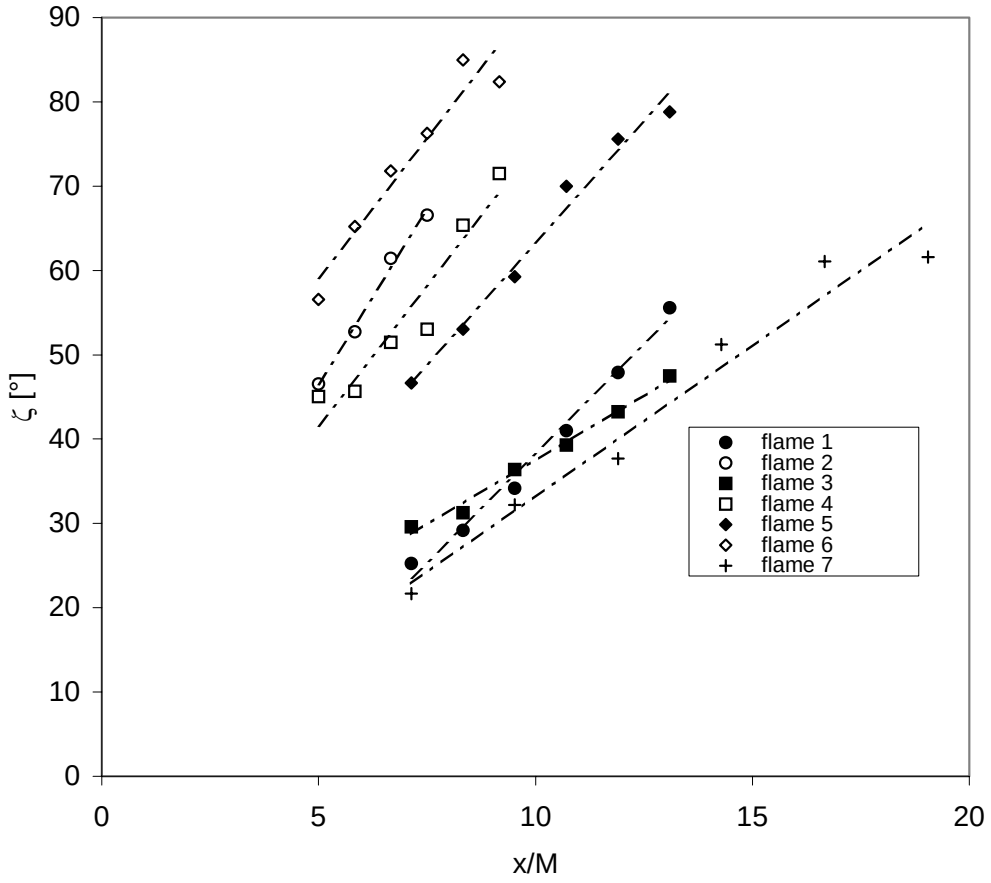

Figure 2.7: Plot of ζ versus x/M for the seven flames studied. Linear curve, least-squares fits of the data are shown in the figure. Their R^2 values range from 0.9144-0.9913. χ^2, the uncertainty associated with ζ, ranges from 0.00001-0.0001.

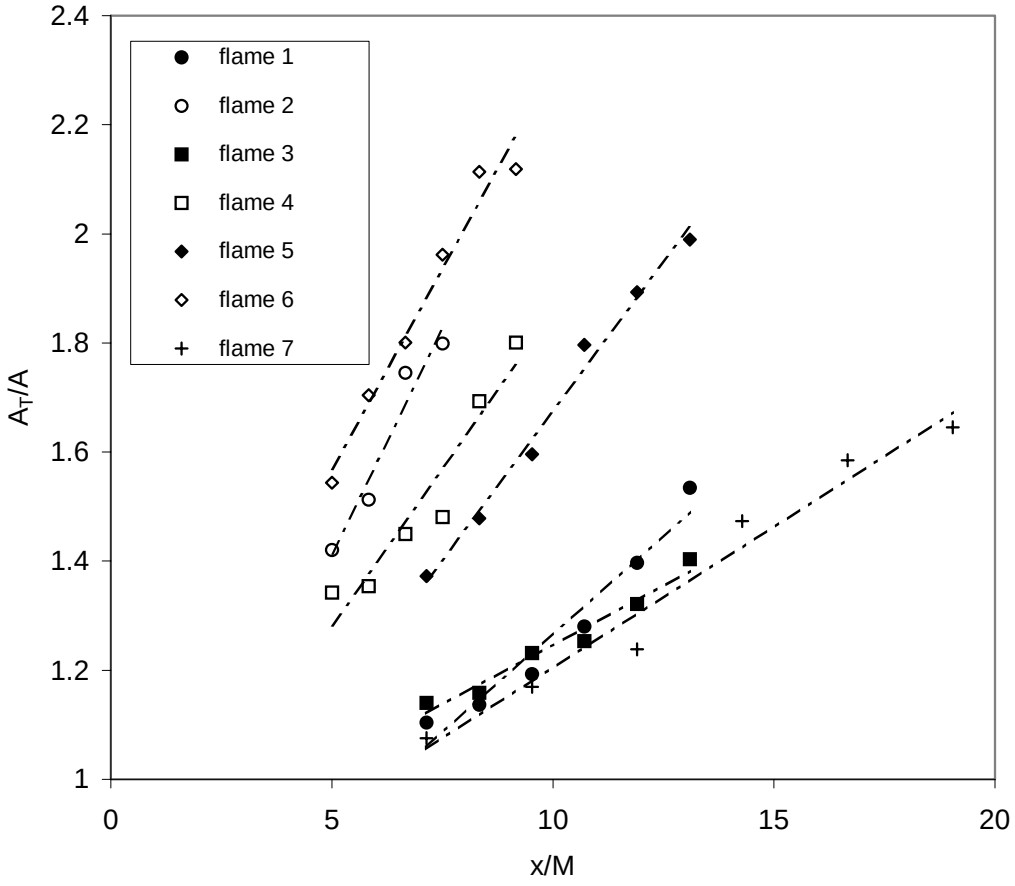

Figure 2.8: Plot of the area ratio, A_T/A, versus x/M for the seven flames studied. The dashed lines are straight line least squares fits of the data. The area ratio is the integral of the surface density along η and hence is a function of ζ and N_C.

indicate the range of u'/S^o_L over which the growth rates are determined. This plot shows considerable scattering indicating that while u'/S^o_L is an important factor determining growth there are other ones.

Flame pairs 1 and 2, 3 and 4, and 5 and 6 each have the same equivalence ratio and bulk velocity but different turbulence generator. For these pairs, growth rate increases with increasing turbulence. Flame 2 has the largest growth rate but not the largest u'/S^o_L. Images show that there is a large amount of lateral movement of the flamelet for flame 2 suggesting that this flame may be influenced by the co-flow. However velocity measurements with and without a co-flow show no effect of the co-flow on velocity fluctuation levels [31] for certain regions of the flame. It has been suggested that thermo-diffusive instabilities can enhance flamelet wrinkling. However previous measurements on V-flames with different Markstein number show no effect [27]. In addition, the range of Markstein for the present measurements is small (Ma = - 0.41 to 0.56) based on results of Reference [35].

Following the work of Gülder cited above attempts were made to correlate growth rate with Re_M and alternately with $(u'/S^0_L)^{1/2}Re_M^{1/4}$ but to no avail. Other factors can be suggested as possible influences on growth rate. They include buoyancy that might explain the high rate of growth of flame 2 which has a low momentum flux and global flow characteristics that influence local values of Σ and thereby Σ formation rates. Trouve and Poinsot [36] have proposed a model equation for Σ that contains a turbulent diffusion term of the form $\nabla \bullet (D_t \nabla \Sigma)$. Arguing by analogy with laminar flames, one can suggest that mean flow stretch can influence Σ in a way analogous to flow stretch in laminar flames. Such effects have not been considered important in the past, but we think merit consideration now.

Summary

Previous crossed-plane imaging measurements of flamelet normal distributions

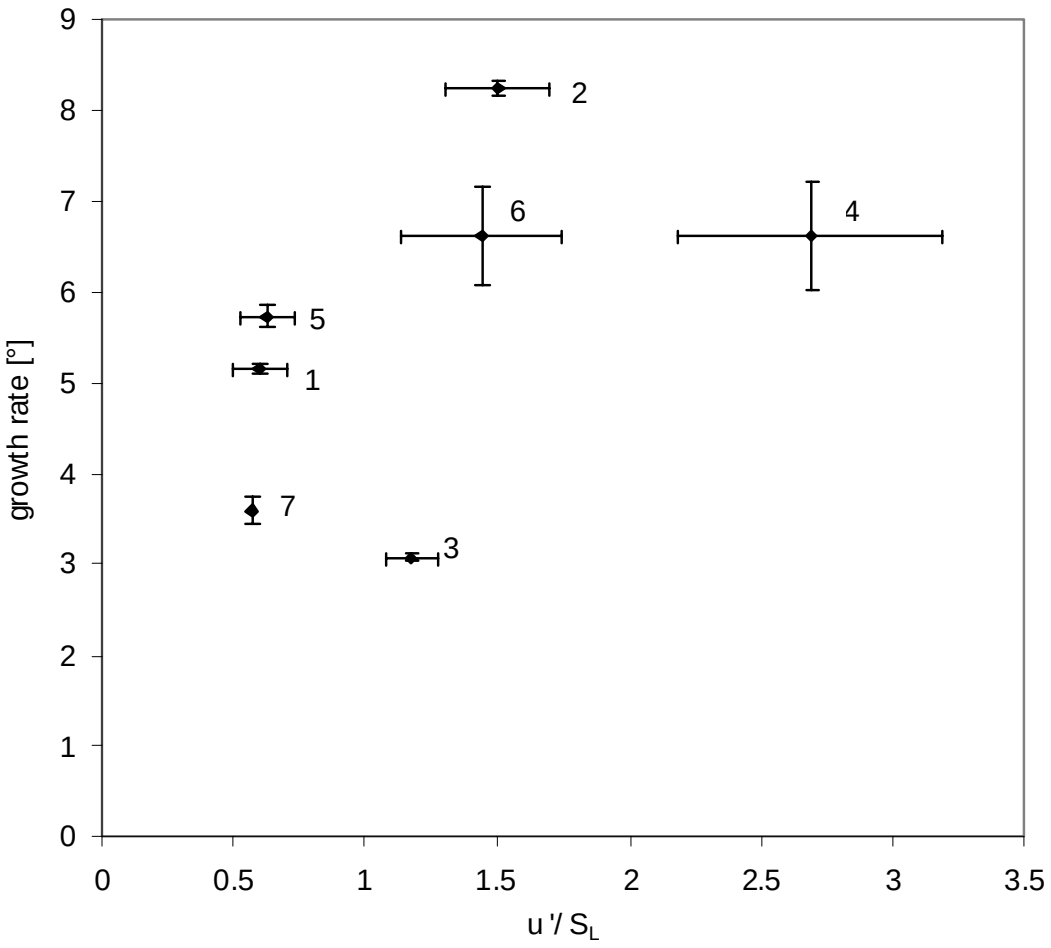

Figure 2.9: Plot of the growth rate of wrinkling quantified by the derivative of ζ with respect to x/M. The numbers in the plot identify the flames. The horizontal error bars indicate the range of u'/S^o_L over which the growth rates are determined. The vertical error bars shown indicate the uncertainty associated with the linear fits of ζ with respect to x. The general trend is for growth rate to increase with increasing u'/S_L^o.

show that these distributions have a simple form with a single fit parameter, Eq. 1.3. This form has been used to obtain a relationship between the three-dimensional fit parameter ζ and its two-dimensional counter part γ describing the PDF of the projection of the surface normal onto a plane that is perpendicular to $<c>$ constant surfaces. The orientation of this projection is defined by its angle with respect to a line perpendicular to <c> constant surfaces.

The relationship between ζ and γ is exploited in order to measure ζ and other important parameters from single plane data as a function of distance from the stabilizer rod in seven methane-air V-flames. The data obtained are used to determine how ζ, N_c and the area ratio A_T/A vary with downstream distance from the stabilizer rod. Substantial, linear variations of ζ and A_T/A are seen in all flames. This result suggests that local burning rates in wake flames, e.g., bluff body-stabilized flames, vary with downstream distance and cannot be quantified by a single number. Growth rates in ζ and A_T/A vary considerably from flame to flame, and the differences cannot be correlated solely by changes in u'/S^o_L. Thermo-diffusive instability is not a factor since Markstein numbers for the flames studies are similar and previous measurements in V-flames showed no such dependency on Markstein number [27]. It is suggested that some of the change is due to mean flow suppression of surface production, stretch effects. The relationship between ζ and γ is applicable to any flame where Eq. 1.2 is satisfied, and it is hoped that the present work will stimulate others to apply single plane imaging to measure the ζ fit parameter in many different flame configurations.

CHAPTER 3

THE COMBINED CROSSED-PLANE LASER TOMOGRAPHY AND SPIV METHOD

Introduction

The purpose of the work described in this chapter is to extend the crossed-plane imaging technique to describe the simultaneous measurement of the instantaneous three-dimensional velocity field in reactants, flamelet surface normal vectors, and for the first time the instantaneous three dimensional flamelet displacement speed relative to reactants. This technique involves combined measurements using stereo particle image velocimetry (SPIV) and crossed-plane imaging.

The turbulent flame speed, or "displacement speed", is a useful measure of the turbulent combustion rate in premixed flames and is analogous to the burning velocity or flame speed of laminar flames. The displacement speed, S_L^d, is defined as the component of the reactant velocity relative to and perpendicular to the flamelet. In the case of a steady, unstretched premixed laminar flame, the flame structure is planar and the reactant flow is steady with zero divergence. Consequently, the component of the reactant velocity perpendicular to the flame and the displacement speed are easily defined, and the displacement speed equals the unstretched laminar burning velocity, S_L^o. In a turbulent flame, the flow is unsteady and the flamelet is curved and strained rendering both the definition of the displacement speed and its relationship to the local stretched burning velocity[1] ambiguous. However, for the range of turbulence conditions in which chemical reactions and scalar quantities can be assumed to be confined to thin sheets, i.e. flamelets, the local displacement speed of a flamelet can be

[1] In this case we define the stretched burning velocity as the burning rate integral [8] divided by the density of the reactants.

measured.

The flamelet displacement speed is defined here as the component of the instantaneous reactant velocity relative to the flamelet (measured at the flamelet surface) and perpendicular to the instantaneous flamelet surface, as determined by crossed-plane tomography. This chapter will describe the combined Crossed-Plane Laser Tomography and SPIV method that is used to measure the flamelet displacement speed. The Crossed-Plane Laser Tomography method is used to find the flamelet normal vector $\underline{N}$. Reactant velocities are measured using SPIV. These quantities are combined with the measurement of the flamelet displacement in the laboratory reference frame to determine the flamelet displacement speed relative to reactants. This is an important quantity because differences between measured displacement speeds and the unstretched laminar burning velocity is an important measure of the impact of turbulence on the structure of of the flamelet.

The displacement speed of steady and unsteady stretched laminar flames and of flamelets embedded in a turbulent flow has been the subject of much interest. For example, Poinsot et al [37] have analyzed a stretched laminar flame and suggested an expression for S_L^d in terms of the Markstein (Ma) and Karlovitz (Ka) numbers: $S_L^d/S_L^o = (1\text{-MaKa})^{-1}$. Hirasawa et al [38] have measured displacement speeds in an unsteady stagnation flame to assess the combined effects of strain and unsteadiness. Sinibaldi et el [39] report displacement speed measurements of a freely propagating laminar flame interacting with a vortex using shadowgraph cinematography and particle image velocimetry. DNS studies have also been performed such as the two-dimensional simulations reported by Chen and Im [40]. As noted by Sinibaldi et al [75] displacement speed measurements in premixed turbulent flames are difficult and have not yet been done because they require the simultaneous measurement of reactant velocity, flamelet speed in the laboratory frame and the flamelet normal vector, $\underline{N}$. By

combining Crossed-Plane Laser Tomography (CPLT) and stereo particle image velocimetry (SPIV) and staggering in time the tomography and SPIV laser pulses we are able to measure all three of these quantities and for the first time report the instantaneous three dimensional flamelet displacement speed.

Combined CPLT and SPIV measurement method

At Cornell we have developed a dual plane imaging method, crossed-plane imaging, in order to measure $\underline{N}$ directly in three dimensions [21, 25-29]. The crossed-plane imaging technique used to find $\underline{N}$ involves simultaneous orthogonal, single plane imaging measurements. Two orthogonal laser sheets define the orthogonal imaging planes. The laser sheets intersect along a line referred to as the measurement line. Reactants are seeded with micron sized silicone oil droplets that are destroyed near the 650 K isotherm thereby marking a flamelet surface that is approximately this isotherm. Where the flamelet crosses the measurement line, three-dimensional flamelet orientation data can be measured. Repeated measurements are made to build a set of $\underline{N}$ and crossing density, n_c, data.

With $\underline{N}$ specified in spherical coordinates by a polar angle, φ, and an azimuthal angle, θ, and the polar axis chosen to be normal to $\langle c \rangle$ constant surfaces (i.e. aligned with η), the crossing-weighted probability density function (PDF) of $\underline{N}$ is

$$P_c(\theta,\phi)d\Omega(\theta,\phi) = C\left|\cos\phi\right|\exp-(\phi/\zeta)^2 \sin\phi d\phi d\theta \qquad (3.1)$$

where the line crossed is the polar axis and $d\Omega(\theta,\varphi)$ is the differential solid angle $\sin\varphi d\varphi d\theta$. According to Eq. (3.1) the PDF of $\underline{N}$ is independent of θ, quasi-Gaussian in φ, and depends on a single fit parameter ζ; C is a normalization constant [21].

With oil seed, PIV images can be used to obtain both velocity distributions in the reactants and images that can be used for measuring $\underline{N}$ via crossed-plane tomography. Traditional PIV yields the in-illumination-plane components of the

velocity of seed particles [41]. Stereo PIV (SPIV), as used here, involves two cameras viewing the same illumination plane [42]. Each camera records an image pair separated by a short time interval and views the same region of the flame from a different perspective. Based on these different views of particle displacements, all three components of particle velocity can be evaluated from the combined image pairs of the two cameras.

Particle velocities are measured by SPIV, based on Mie scattering from the seed particles, so that, for the present case, velocity measurements are restricted to regions where the temperature is below approximately 650 K. The seed particle velocities are measured within the SPIV illumination plane. Particle velocities are measured near the flamelet surface as defined by seed particle evaporation in the preheat region of the flame, a region where temperature gradients are large (~10,000K/cm). SPIV relies on tracking the seed particles over a fixed time interval to measure the flow velocity. It is often assumed that the seed particles travel at the same velocity as the reactant flow. However, seed particle velocities can lag behind the reactant flow because of inertia and because of thermophoretic forces. Chapter 4 describes the formulation of the thermophoretic force correction needed for seeded flow in regions of high temperature gradients to obtain the gas velocity.

The flamelet displacement speed observed in the laboratory frame, S_L, is also needed. S_L is defined such that it is positive for motion towards reactants. S_L is obtained from measurements of the flamelet displacement along the measurement line, Δx, during a time period Δt, the time between the tomography laser pulse and the first SPIV laser pulse. This displacement is determined by comparing the flamelet position on the measurement line in a tomography image with its position on the measurement line in the associated SPIV camera image obtained Δt later. To see how S_L is obtained from Δx consider the flame surface displacement perpendicular to itself, d, over time

Δt viewed in a plane containing the measurement line, defined by the unit vector $\underline{N}_L$ pointed in the direction of laser propagation, and $\underline{N}$ in Figure 3.1. S_L is the flamelet speed perpendicular to itself and is given by $d/\Delta t$. It follows from the geometry portrayed in Figure 3.1 that $S_L = \Delta x\ (\underline{N} \bullet \underline{N}_L)/\Delta t$. For this measurement it is assumed that, over the time Δt and within a volume swept out by the motion of the flamelet along the measurement lines during Δt, the flamelet is planar, moves at a constant speed and does not rotate.

Note that the sign of S_L is physically significant. If S_L is positive the flame surface is moving relative to the laboratory in the direction of the normal. If it is negative, the flame is moving in a direction opposite to that of the normal. Thus the sign of d is important; it is negative when $x_2 < x_1$ and $(\underline{N} \bullet \underline{N}_L)$ is positive and when $x_2 > x_1$ and $(\underline{N} \bullet \underline{N}_L)$ is negative.

Determination of the displacement speed, S_L^d, from measured quantities

In addition to the above measurements of reactant velocity, $\underline{N}$, and S_L, the flamelet displacement speed relative to the reactants, S_L^d, can be measured using the crossed-plane tomography and SPIV images. For this, the vertical SPIV plane is aligned perpendicular to the flame-stabilizing rod. A laser is used to illuminate two tomography scattering planes oriented at 45° angles with respect to the SPIV measurement plane. These two planes and the SPIV plane intersect along three horizontal lines, the measurement lines. The tomography image set is separated by a short time interval from the SPIV image set, and the flamelet position along the measurement lines is measured in each image. The flamelet surface displacement speed S_L is observed along the measurement lines and is evaluated based on the flamelet displacement between the image sets and the time interval between laser pulses.

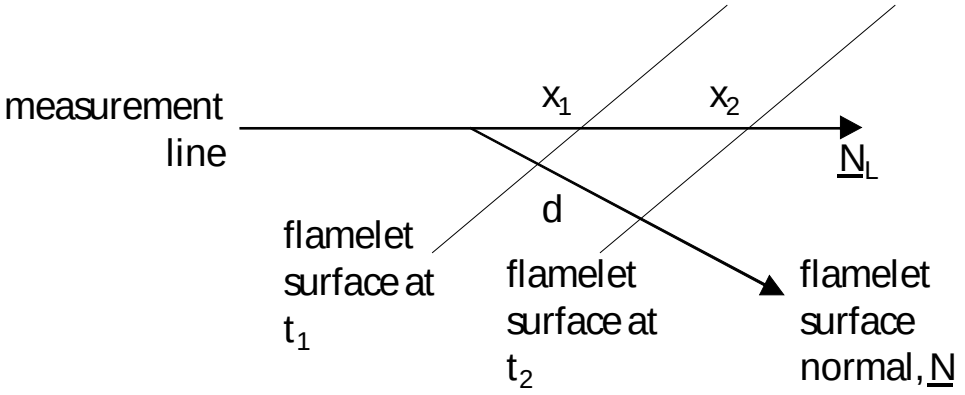

Figure 3.1: Displacement of the flamelet along the measurement line in a time $t_2 - t_1$ as seen in the plane defined by the unit vector $\underline{N}_L$, and the flamelet surface normal.

S_L^d is defined as the relative velocity between the flamelet surface (approximately the 650 K isotherm) at the measurement point and the reactants next to that point. The flamelet surface can only move perpendicular to itself. If S_L is defined such that it is positive for motion towards reactants, then the flame surface velocity vector in the laboratory frame is $S_L\underline{N}$. Let $\underline{U}_r$ be the reactant velocity at the flamelet surface, it follows that $S_L^d = (\underline{U}_r - S_L\underline{N})\bullet\underline{N}$.

Next steps

The next chapter discusses the thermophoretic force and the importance of its consideration on SPIV measurements. The accuracy of laser imaging techniques for measuring fluid velocities in seeded flows (such as laser-Doppler velocimetry and SPIV) depends on how closely the seeding particles follow the flow. The thermophoretic force is the force that a particle feels as it travels through regions of high temperature gradients. In these regions, the molecules on the hotter side of a seed particle have on average higher momenta than those on the cooler side of the seed particle, resulting in a net force on the particle in the direction of decreasing temperature. This chapter describes the formulation of the thermophoretic force correction for seeded flow in regions of high temperature gradients.

Chapter 5 describes the results of using the combined CPLT and SPIV technique on a premixed turbulent methane-air V-flame. The instantaneous flamelet surface normal vector ($\underline{N}$), the three dimensional reactant velocity vector fields and the flamelet displacement speed obtained by a combination of crossed-plane tomography and SPIV are presented here for the first time. SPIV is used to measure the reactant velocity field in the vertical plane. Flamelet normal vectors are obtained where the flamelet intersects the measurement lines. Two measurement lines are in the SPIV

plane and where the flamelet intersects these lines we simultaneously measure $\underline{N}$ and the reactant velocity. In addition, the flamelet displacement speed is measured in the laboratory frame and with respect to the reactants. Data for these latter quantities are reported here for the first time. As noted flamelet displacement speed data are important to quantifying and understanding the impact of the turbulent velocity field on the preheat zone of the flamelet.

Chapter 6 analyzes the individual sources of uncertainty in the combined crossed-plane tomography method and discusses the calculated uncertainty in the flamelet displacement speed measurements. The individual sources of error in the measurement method are identified and discussed. The propagation of individual measurement error to the calculated uncertainty in the flamelet displacement speed is also discussed in this chapter.

CHAPTER 4

SPIV AND THERMOPHORESIS

The Thermophoretic Force

The accuracy of laser imaging techniques for measuring fluid velocities in seeded flows (e.g. laser-Doppler velocimetry and SPIV) depends on how closely the seeding particles follow the flow. Doing a force balance on a seed particle, there is viscous drag (which causes the particle to follow the fluid motion), inertial, electrostatic, gravitational, centrifugal, acoustic, diffusiophoretic, photophoretic, and thermophoretic forces – all of which cause the motion of the seed particle to depart from the flow velocity [43]. Among these, only viscous drag, inertia and thermophoresis are significant in typical reacting flows, which have high temperature gradients. Errors attributable to particle inertia effects have been widely studied. Haghgooie et al [44] and Melling [45] found that for LDV and PIV techniques in turbulent non-reacting flows (where viscous drag and inertial forces are important, but the thermophoretic force is small), particles of 1 or 2 microns in diameter should adequately follow velocity fluctuations in the flow. However, in reacting flows it is found [46, 47] that for even small particles, the particle lag in the reaction zone is appreciable.

The thermophoretic force is the force that a particle feels as it travels through regions of high temperature gradients. In these regions, the molecules on the hotter side of a seed particle have, on average, higher momenta than those on the cooler side of the seed particle, resulting in a net force on the particle in the direction of decreasing temperature. The following is the formulation of the thermophoretic force correction for seeded flow in regions of high temperature gradients.

From Sung et al [48] the equation that describes particle motion is

$$m_p \frac{du_p}{dt} = F_{SD} + F_{TP} = F_{AT} \tag{4.1}$$

where $m_p=\rho_p\pi d_p^3/6$ is the particle mass, ρ_p is the particle density, d_p is the particle diameter, u_p is the particle velocity, t is time, F_{SD} is the Stokes drag force, F_{TP} is the thermophoretic force and F_{AT} is the particle inertial force. The particles are assumed to be spherical. The Stokes drag force is the drag force exerted on a particle in low Reynolds number flow [49],

$$F_{SD} = -3\pi\mu d_p (u_p - u_f), \tag{4.2}$$

where μ is the fluid viscosity and u_f is the local fluid velocity. Sung et al [48] have introduced a slip-factor to account for Knudsen number effects, which are important for micron-sized particles:

$$F'_{SD} = \frac{-3\pi\mu d_p (u_p - u_f)}{C_{KW}} = B \tag{4.3}$$

and

$$C_{KW} = 1 + Kn\left[\alpha + \beta \exp(-\gamma / Kn)\right] \tag{4.4}$$

is the Knudsen-Weber form of the slip-correction factor. $Kn=2\lambda/d_p$ where Kn is the Knudsen number and λ is the viscosity-based value for the mean free path of the gas molecules [50],

$$\lambda = \frac{2\mu}{\rho_f \bar{c}} \tag{4.5}$$

where ρ_f is the fluid density and

$$\bar{c} = \sqrt{\frac{8R_g T}{\pi}} \tag{4.6}$$

where R_g is the specific gas constant and T is the fluid temperature. The constants α, β and γ are found by fitting the Knudsen-Weber equation to the experimental data of Allen and Raabe [50], α=1.142, β=0.558 and γ=0.999.

In the slip-flow (Kn<1) to the free molecular flow limit (Kn→∞), the thermophoretic force on a spherical particle due to a temperature gradient can be expressed as [50, 52]

$$F_{TP} = -\frac{6\pi\mu\nu_p d_p C_S\left(\kappa_f/\kappa_p + C_t Kn\right)}{\left(1+3C_m Kn\right)\left(1+2\kappa_f/\kappa_p + 2C_t Kn\right)}\frac{\nabla T}{T} = -A\frac{\nabla T}{T} \tag{4.7}$$

where ν_p is the droplet kinematic viscosity, κ_f and κ_p are the fluid and particle thermal conductivities, respectively, and C_s=1.17, C_m=1.14, and C_t=2.18 are the thermal slip, momentum exchange, and thermal exchange coefficients specified by the kinetic theory of gases [50]. For polyatomic gases, the translational component of thermal conductivity should be used, $\kappa_f=\kappa_{tr}$. If $\kappa_f=\kappa_{tr}$ is small compared to κ_p, F_{TP} reduces to

$$F_{TP} = -\frac{6\pi\mu\nu d_p C_S\left(C_t Kn\right)}{\left(1+3C_m Kn\right)\left(1+2C_t Kn\right)}\frac{\nabla T}{T} = -A'\frac{\nabla T}{T} \tag{4.8}$$

Correction for Thermophoresis – Analysis and assumptions

A numerical calculation was used to find an estimate of F_{TP} in the reaction zone of the turbulent premixed flame that was studied here using the combined crossed-plane laser tomography and SPIV method. In a stationary, unstrained, planar, laminar, premixed, lean (φ_{equiv}=0.65) methane-air flame, we can consider a force

balance on the seed particles, neglecting particle-particle collisions. Particles are micron sized silicone oil droplets that evaporate at 650 K. For this flame the Knudsen number for the droplets was calculated at T=650 K such that μ=3.23e-5 Ns/m^2 [31] and Kn=0.3. For a first-order approximation, we assume that the particles are traveling at the reactant flow velocity as they enter the flame – an unstrained, planar steady flame – so the velocity component perpendicular to the flame is S^o_L. No forces act on the particles in the tangential direction, and consequently the particles follow the direction of the flow perpendicular to the flame. The only forces to consider are those perpendicular to the flame – the viscous drag force, inertia and thermophoresis. The force balance becomes:

$$m_p \frac{du_p}{dt} = F_{SD} + F_{TP} = -B(u_p - u_f) - C\frac{\nabla T}{T} \tag{4.10}$$

where C represents A or A' from the above expressions of F_{TP}. Eq. 4.10 can be non-dimensionalized with velocity, length and time scales given by S^o_L, α/ S^o_L and $\alpha/ S^o_L{}^2$, where α is the thermal diffusivity:

$$u = \frac{u_p}{S_L^o} \tag{4.11}$$

$$\nu = \frac{u_f}{S_L^o}$$

$$\tau = \frac{t}{\alpha / S_L^{o\,2}}$$

$$b = -(B/m_p)(\alpha / S_L^{o\,2})$$

$$a = -(A/m_p)\nabla T / T(\alpha / S_L^{o\,3})$$

$$\chi = \frac{x}{\alpha / S_L^o}$$

In non-dimensional terms the equation for particle velocity is

$$\frac{du}{d\tau} = b(u - \nu) + a \tag{4.12}$$

a and *b* depend on gas property values and the flame structure (e.g. S^o_L, T and ∇T). S^o_L, T, ρ and u_f versus x are determined from Reaction Design Chemkin 4.1 Premix [53] calculations of a lean methane-air flame (φ_{equiv}=0.65) using Chemkin's reduced mechanism. The position in the flame where x=0 is at T=298K in the reactants away from the reaction zone. The Chemkin calculation outputs contain only temperature, velocity, density, enthalpy, and species mole fractions as a function of x. In conjunction with Chemkin, Cantera [54] was used to determine the thermal conductivity, k, and heat capacity, c_p, in order to find the thermal diffusivity (α=k/ρc_p) of the mixture. Gas properties were calculated for the unreacted mixture in the temperature interval of 300<T<1000K, the temperature interval from the Chemkin calculation.

A, A' and B were calculated quantitatively by calculating A(T), A'(T) and B(T), mapping these functions onto the structure of the flame found using Chemkin, and numerically solving the differential equation, eq. 4.12. For this methane-air flame model, κ_f=κ_{tr}=0.05 W/mK is small compared to κ_p=0.3 W/mK, and F_{TP} reduces to Eq. 4.8. Third order polynomial fits of A' and B versus temperature were made over the temperature range around the 650 K isotherm (450<T< 900 K), Fig. 4.1. These fits are used to map A' and B as functions of T onto the structure of the Chemkin-calculated methane-air flame. a' and b (the non-dimensionalized forms of A' and B) were calculated and plotted against the non-dimensional spatial coordinate, χ. To compute the particle velocity within the flame, polynomial fits of a' and b versus χ were made for 1.05<χ<1.3 (450<T<900K), see Fig. 4.2. For χ outside of this range, good polynomial fits are not possible; thus these calculations are good only in the preheat zone of the flame. For this model, the thermophoretic force correction is

Table 4.1: Summary of parameters used in calculating the thermophoretic velocity correction for the modeled flame.

Parameter	Units	Value
m_p	kg	5.01e-16
ρ_p	kg/m^3	957
d_p	m	1e-6
μ	Ns/m^2	3.23e-5
$Kn_{particle}$		0.3
ρ_f	kg/m^3	0.5356
R_g	$(m/s)^2(1/K)$	690
λ	m	1.79e-4
φ_{equiv}		0.65
α	m^2/s	8.65e-5
$Kn_{particle}$		0.3
ν	m^2/s	6.021e-6
S_L^o	m/s	0.126
c_p	kJ/kgK	1.063
C_{KW}		1.41
A’		$\frac{6\pi\mu\nu d_p C_s C_t Kn}{(1+3C_m Kn)(1+2C_t Kn)}$
B		$\frac{-3\pi\mu d_p (u_p - u_f)}{C_{KW}}$
C_m		1.14
C_s		1.17
C_t		2.18

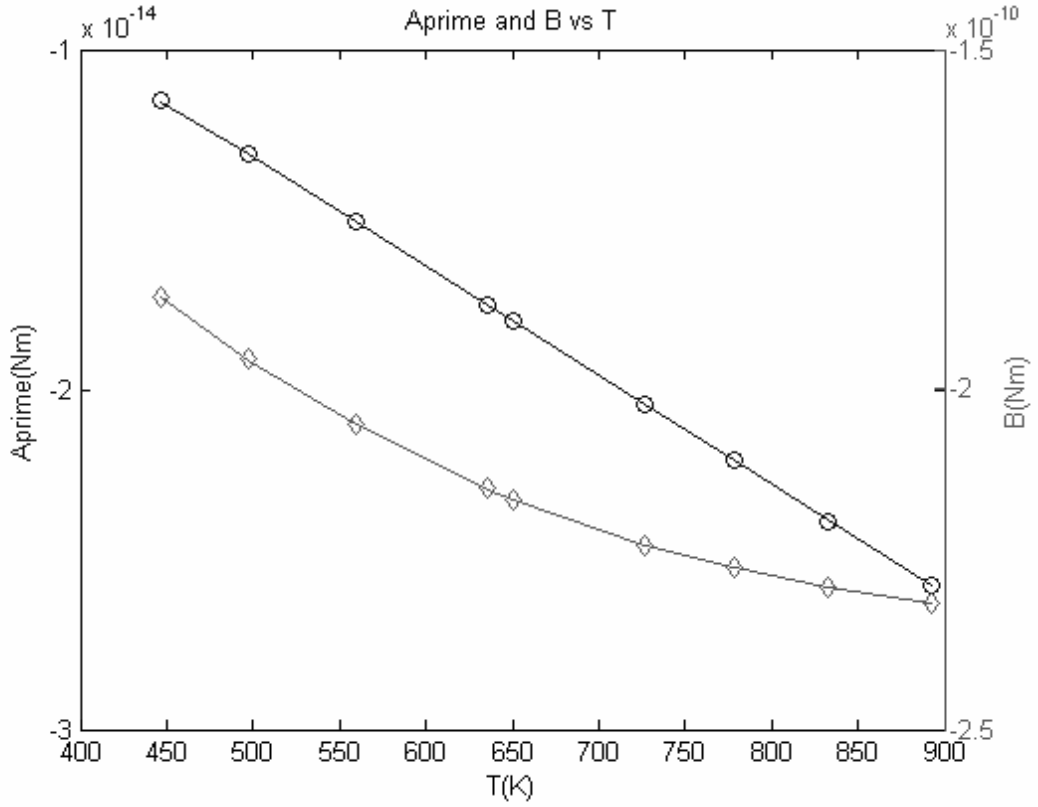

Figure 4.1: Plots and fits of A' (circles) and B (diamonds) versus T in a lean (φ_{equiv}=0.65) methane-air flame. Third order polynomial fits of A' and B versus temperature were made over the temperature range around the 650 K isotherm (450<T< 900 K).

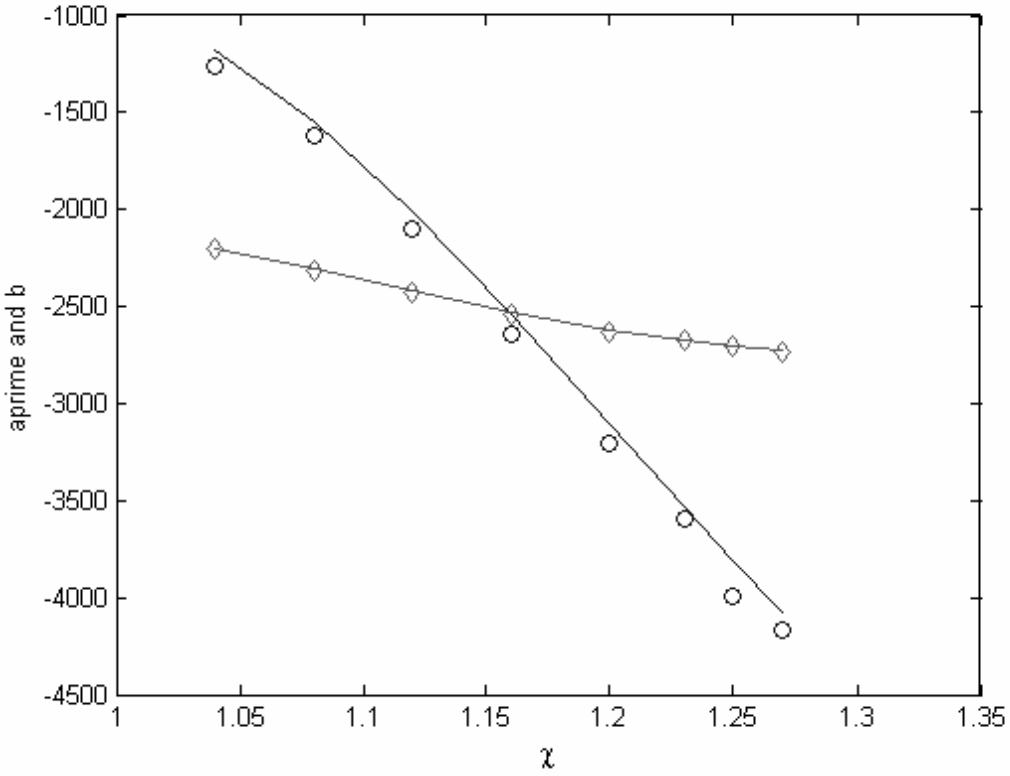

Figure 4.2: Plots and fits of a' (circles) and b (diamonds), the non-dimensionalized forms of A' and B, versus χ, the non-dimensional spatial coordinate, in the preheat zone of a lean (φ_{equiv}=0.65) methane-air flame. The fits of A' and B are used to map A' and B as functions of T onto the structure of the Chemkin-calculated methane-air flame. a' and b were obtained and plotted against χ.

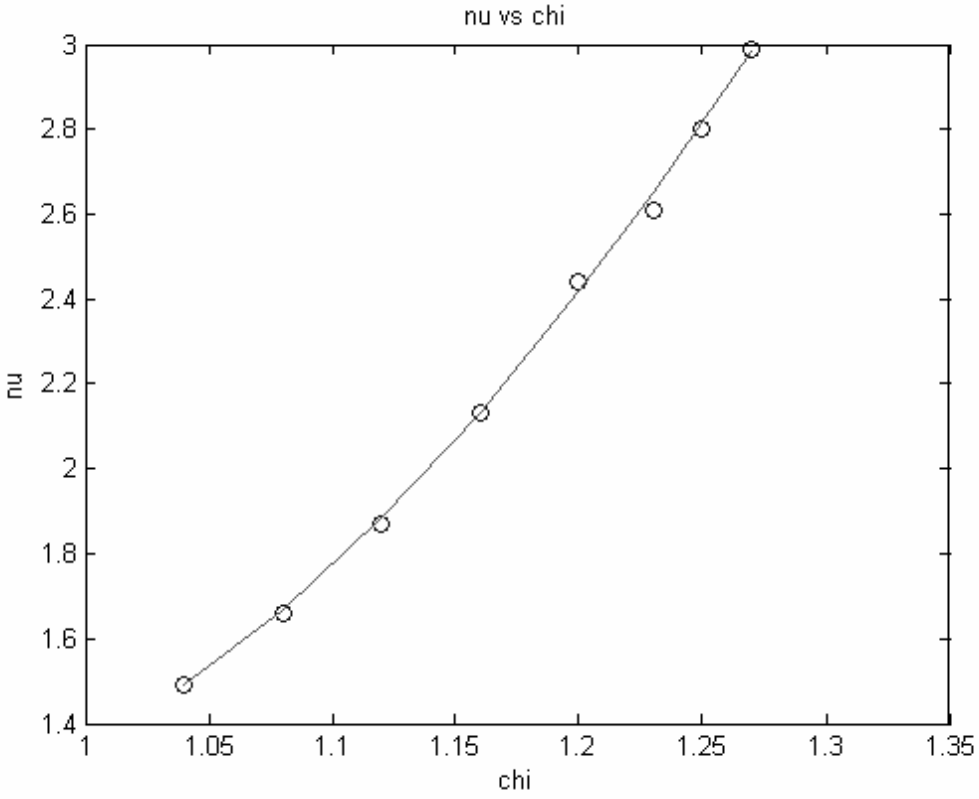

Figure 4.3: Plot and fit of $\nu=f(\chi)$, the non-dimensional fluid velocity versus χ, the non-dimensional spatial coordinate, in the preheat zone of a lean (φ_{equiv}=0.65) methane-air flame.

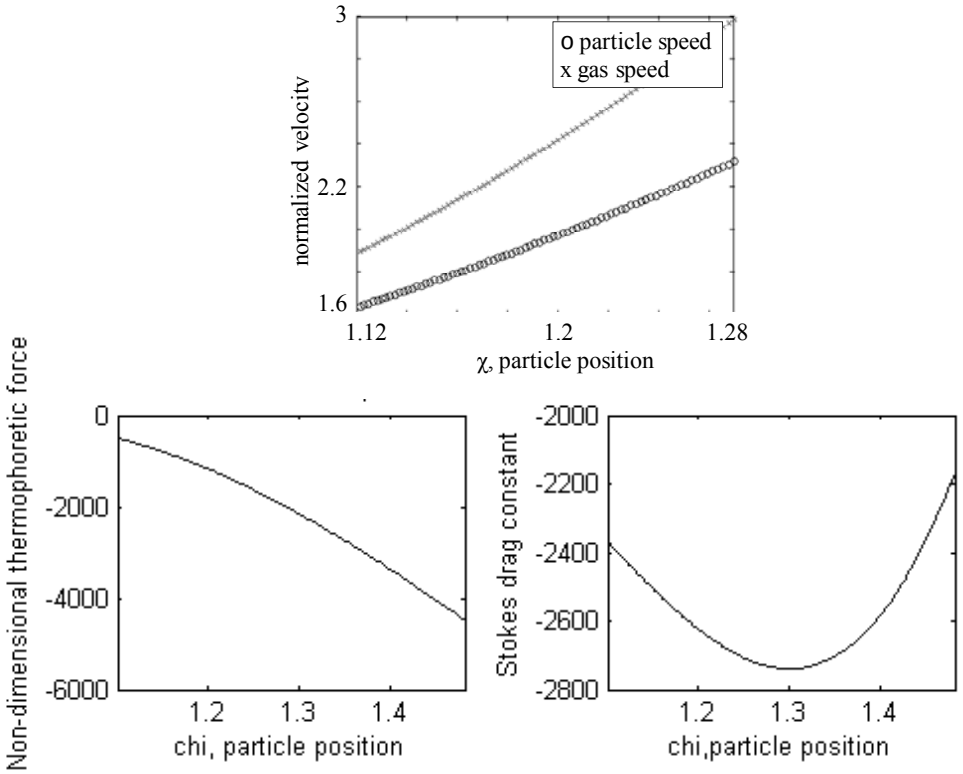

Figure 4.4: Plots of particle speed, gas speed, the non-dimensional thermophoretic force, and the Stokes drag constant versus χ showing that particle velocity acceleration across the flame lags that of the gas.

needed only in the preheat zone of the flame.

To complete the specification of Eq. 4.12, ν as a function of χ needs to be calculated. By continuity of a one-dimensional flame, $\nu=\rho_o/\rho$. In Figure 4.3, ν is plotted against χ in the preheat zone and fit to a 3rd order polynomial for input to the calculation.

The fits of a', b and ν versus χ are inputs to calculations to solve Eq. 4.12 using the Matlab differential equation solver (ode23). Eq. 4.12 was integrated in time. The location, χ, and velocity, u, of the particle were evaluated at each time step. The initial condition used for this calculation was u=1 at χ =1.1. The ode23 differential equation solver is an implementation of an explicit Runge-Kutta method, and is appropriate to use for moderately stiff problems, such as Eq. 4.12. The results are shown in Fig. 4.4. These results show that because of the large temperature gradient in the preheat region of a flame, thermophoretic forces can cause the motion of seeding particles to lag behind the flow. For this flame, the difference is small but significant.

CHAPTER 5

FLAMELET DISPLACEMENT SPEED MEASUREMENT AND RESULTS

Experimental Apparatus

Combined SPIV and crossed-plane tomography measurements were performed on a V-flame burner, Fig. 5.1. Measurements were made on a lean methane/air flame. The fuel and air flow rates were measured with mass flow meters and used to determine the bulk flow velocity (2 m/s) and the equivalence ratio (φ_{equiv}=0.65). A portion of the air flow was diverted through a blast-atomizer type seed particle generator, within which the flow is seeded with silicone oil droplets, and then passed through a cyclone separator. Droplet sizes were estimated to be no more than a few microns in diameter [31]. The mean droplet diameter is 1 micron, with a small number of larger droplets, up to 5 microns, expected as well. The reactants were mixed in a plenum at the base of the burner. Turbulence was generated by a wire mesh grid positioned 50 mm upstream from the stabilizing rod. The grid had approximately 4.5 squares/cm^2, a 0.86 mm wire diameter, and a mesh spacing, M, of 4.2 mm. *u'*, the turbulence intensity, at the measurement location in cold flow was 0.2 m/s, as measured by the SPIV system. Measurements were made 40 mm downstream from the flame-stabilizing rod, which was located at the burner exit. To reduce interference from light scattered by room air dust, the premixed flame was sheathed by a coaxial flow having a velocity similar to that of the reactant flow.

For the combined measurements a frequency doubled, pulsed Nd:YAG laser (the tomography laser), was used to illuminate two orthogonal scattering planes oriented at 45° angles with respect to a vertical plane that was aligned perpendicular to the stabilizing rod of the V-flame, Figs. 5.2, 5.3. The tomography laser beam was split into two beams and then formed into two thin orthogonal sheets that supply the

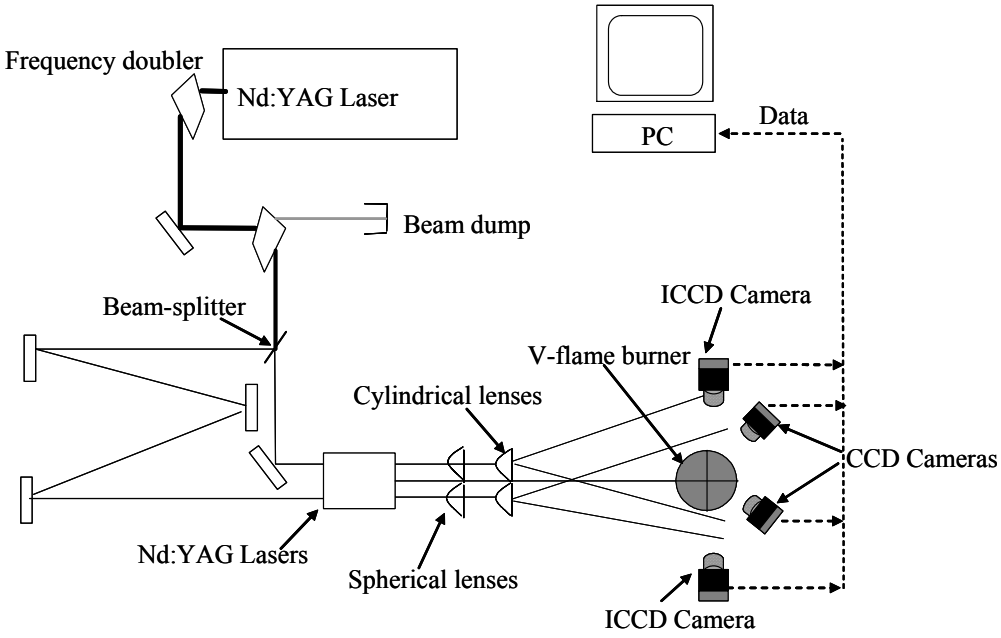

Figure 5.1: Schematic diagram of combined crossed-plane laser tomography and SPIV apparatus. The tomography laser beam is split via a beam splitter. One tomography laser beam is delayed temporally by a much longer beam path. The three laser sheets (two tomography and one SPIV) intersect over the burner axis. Imaging data are collected by the CCD cameras and are stored for post-processing on a PC.

incident photons for Mie scattering. These sheets define the tomography imaging planes (Fig. 5.3). One beam path was approximately 7 m longer than the other, resulting in a temporal separation in the beams' arrival times at the burner of ~25 ns. The SPIV measurements were made in a vertical plane aligned perpendicular to the stabilizing rod of the V-flame. Two frequency doubled, pulsed Nd:YAG lasers were used to illuminate this plane. The crossed plane tomography and SPIV laser sheets are less than 0.2 mm thick. The sheet thickness was measured by imaging a reflection of the sheet at low laser power onto a CCD [55].

The lasers fired in a time sequence where the tomography laser fired first, then the first SPIV laser fired 1.5 ms later, and the second SPIV laser fired 42 μs after the first one. The tomography ICCD camera intensifiers are used as electronic shutters so that the cameras can be gated around the tomography beams' arrival times. The delay in arrival time between the first and second tomography beams is 15 ns. The interpulse time between the time when the tomography laser fires and the time when the first SPIV laser fires needs to be tightly controlled, as it determines the Δt measured for the displacement speed in Eq. 3.2. Δt=1.5 ms was selected for this flame because it is on the order of the characteristic time of flamelet motion. The interpulse time between the first and second SPIV laser pulses is also important, as the velocity of the particles are determined by measuring the distance that particles travel between laser pulses and dividing by the interpulse time. A SPIV interpulse time of 42 μs was chosen such that most particle displacements could be measured in the SPIV image. Laser timing jitter is estimated to be ~ 1 μs, based on information from the manufacturers of the SPIV control box, which controls the timing of the SPIV and tomography lasers [56]. The SPIV laser beams were formed into thin sheets for Mie scattering to define the SPIV imaging plane. The SPIV measurement plane was displaced horizontally 1 mm from the intersection of the tomography illumination

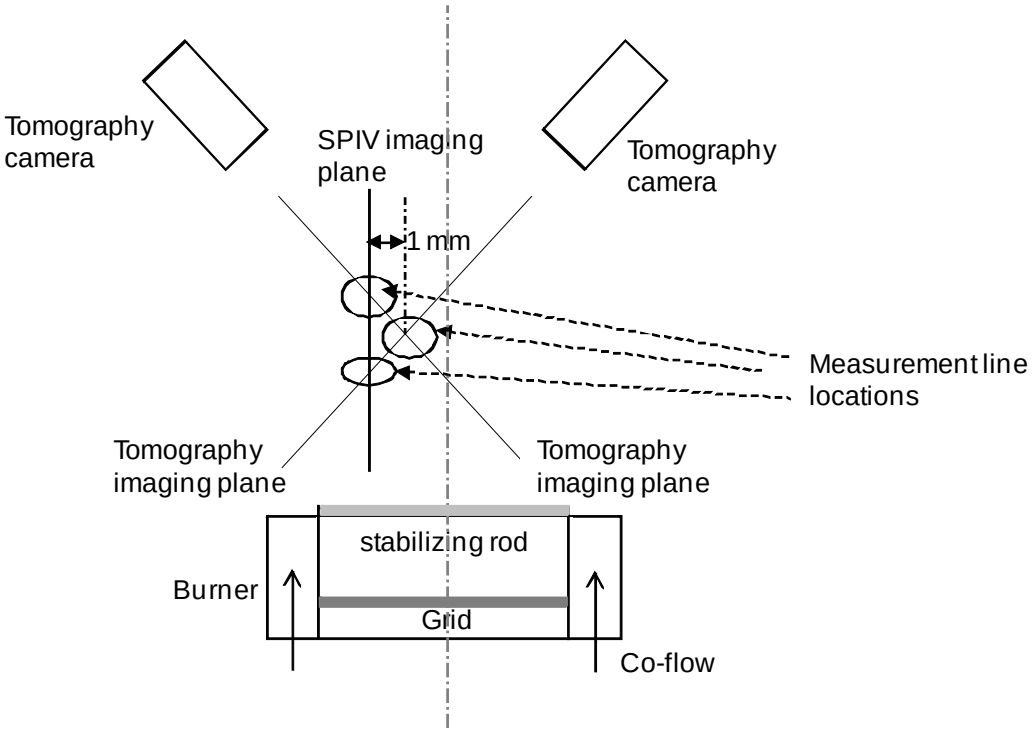

Figure 5.2: Schematic diagram of the V-flame and burner, tomography cameras and imaging planes. The flame is stabilized on a rod placed across the burner exit. The locations of measurement planes in the laboratory reference frame are indicated.

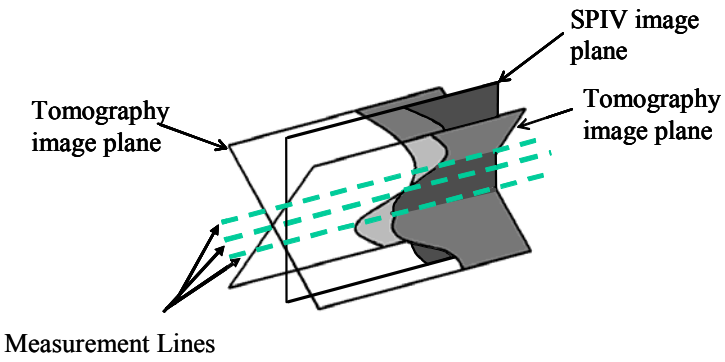

Figure 5.3: Schematic of laser-sheet orientations for combined CPLT and SPIV. The two tomography laser sheets lie at 45° with respect to the vertical SPIV laser sheet. The sheets intersect forming three measurement lines.

planes (Fig. 5.3).

As noted, the reactants were seeded with micrometer sized silicone oil droplets that are consumed within the flamelet such that Mie scattering of laser light occurs in the reactants but not the products, thereby imaging the 650K isotherm [27]. Tomography images were recorded with two ICCD cameras each having a 512 x 512 pixel CCD array. The tomography cameras were positioned perpendicular to the laser sheets, i.e. a sheet is parallel its camera's image plane. The field of view imaged was 40 x 40 mm for each camera, and the cameras have a spatial resolution of better than 0.2 mm. SPIV images were recorded with two CCD cameras each having a 1024 x 1360 square-pixel CCD array. The SPIV cameras were positioned at an angle to the SPIV laser sheets, such that each SPIV camera views the same region of the flame from a different perspective. The field of view imaged was 25 x 35 mm for each camera and the spatial resolution was better than 0.1 mm. The timing sequence for exposing the cameras was initiated by a trigger pulse from the tomography laser.

Image Analysis

Approximately 1500 image sets (2 crossed-plane tomographic images and 4 SPIV images per set) were acquired and saved for image processing. Crossed-plane tomography images are bright in the reactants due to Mie scattering and are dark in the products (Fig. 5.4). The boundary between light and dark regions denotes the intersection of the flamelet surface and the laser illumination plane, the flamelet curve.

To find the flamelet curve in each tomography image, the images were processed beginning with a thresholding step. Changes in contrast between products and reactants can be detected by operators that calculate the gradient of an image. The Sobel operator, a horizontal edge-emphasizing filter [33, 57], was used to calculate the gradient of an image and to create a binary mask based on a specified threshold value.

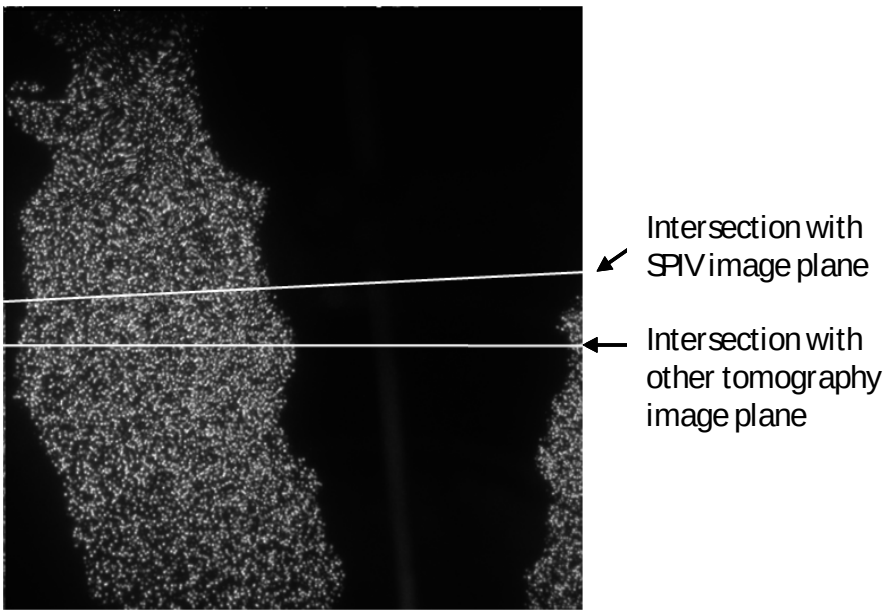

Figure 5.4: Sample tomography image of the turbulent V-flame. Bright pixels indicate cold regions (reactants) where laser photons Mie scatter off of the silicone oil droplets, and dark pixels indicate hot regions (products). The white lines indicate the two measurement lines: the crossing location of SPIV image plane (upper line) and the crossing location of the orthogonal tomography image plane. The area imaged for each tomography image is 40 mm x 40 mm. The area imaged for each SPIV image is 25 mm x 35 mm.

With the mask the image was made binary, and the binary image operations of opening and closing [33] were used to remove noise of scales smaller than the 0.2 mm camera resolution. Flamelet crossings were identified in each tomography image as points where the flamelet curve intersects the measurement lines (the intersection of two laser sheets). A planar transparent target is aligned with the illumination plane containing the measurement line to determine the location of the measurement line. The lasers fired onto the target and gating of the two cameras was switched relative to the laser pulse arrival times so that the cameras imaged scattering from the edge-on sheet off of the target. The edge-on sheets appear as lines in an image and were linearly fit to define their location in the image. Flamelet crossings of these lines were then identified in the images, within an error of 0.2 mm. The flamelet curve was found by an edge-finding algorithm [57] and then was fit locally over a fit-width of 80 pixels to a third order polynomial at each crossing location. From a fit of the flamelet, its slope is determined at flamelet crossing points and is used to define tangent vectors to the flamelet curve in the laser illumination plane. The tangent vectors in the image pairs for a given flamelet crossing are tangent to the flamelet surface. The normalized cross product of the two tangent vectors which is aligned with the flamelet surface normal was taken to find $\underline{N}$. Further details on image processing can be found in [58].

Flamelet surface normals were also found at the intersections of the SPIV illumination plane and the tomography illumination planes. The raw SPIV images were processed for both velocity (see below) and flamelet normal measurements, as described in the paragraph above. For the flamelet normal, the SPIV images were thresholded, making the images binary, followed by the binary operations open and close. The SPIV cameras have a spatial resolution better than 0.1 mm, so that individual particles in the images can be identified. To accommodate this high resolution a different threshold value was used than that used for the tomography

images so that the Sobel operator could calculate a gradient based on the change in contrast between products and reactants and not between particles. The measurement lines in the SPIV image plane correspond to intersections of the SPIV plane with both of the tomography planes. The locations of these lines in the tomography planes and the SPIV plane were determined by imaging scattering from the tomography laser sheets off of a thin planar transparent target aligned by eye with the SPIV laser sheet. The scattered light appeared in the images as lines, and these lines were linearly fit to define the locations of the measurement lines in the SPIV camera images. A registration mark on the transparent target that appears in the camera images was used to define the point of origin for all four cameras. The flamelet curves at the measurement line crossings in each image (SPIV and tomography) were fit locally to a third order polynomial curve to find their tangents.

Because the SPIV cameras were at an angle to the SPIV plane, the SPIV images are distorted. The SPIV calibration target is a precisely machined grid of 5 x 5 holes (25 x 25 mm). The grid was positioned at the SPIV measurement plane (1 mm away from the stabilizing rod) and an image of this grid was used as a reference for correcting the flamelet position and flamelet tangent vectors for the effects of this distortion. The cross product of two corresponding tangent vectors gives the flamelet surface normal. The error in finding the location where the flamelet crosses the measurement line in the SPIV image is 0.2 mm. Error associated with the measurement of $\underline{N}$ is discussed in [37]. Further details on image processing can be found in [25, 27-28].

For the reactant velocity field, SPIV images were recorded and processed using ProVision II version 2.01.05 software (IDT, Tallahassee, Florida). Individual seed particles are discernable in the recorded images; the software evaluates the velocity of these individual particles within a pre-drawn mesh in the image plane. The

mesh used here is 24 x 70 squares measuring 6 x 17 mm, positioned to straddle the measurement lines in the plane of the SPIV laser sheet. The velocity was evaluated based on a calibration performed prior to data acquisition [41]. The three-dimensional particle velocity was extracted along the two measurement lines in the mesh in the SPIV measurement plane. Flamelet crossings were then identified in the reactant velocity field in this mesh. For calculating the displacement speed, the particle velocity was averaged over three mesh points in the velocity field (~0.5 mm) centered where the flamelet curve intersects the measurement line, along the tangent to the flamelet curve in the reactants straddling the measurement line. The particle velocity was averaged over these points to reduce error in the velocity measurements. The averaged value was used as the particle velocity where the flamelet crosses a measurement line in the SPIV plane. Experimental uncertainty in SPIV data ranges from 1-5%, based on test results reported in [42] of an SPIV system in which a test target consisting of hollow glass spheres suspended in a solid clear araldite block was moved on a translation stages to simulate the three dimensional motions of seed particles. See Chapter 6 for more details on determining the experimental uncertainty in the SPIV system.

Implementing the Thermophoretic Force Correction

Reactant velocities are measured by SPIV, where seed particle velocities are measured within the SPIV illumination plane. Particle velocities are measured near the flamelet surface as defined by seed particle evaporation, the 650K isotherm, in the preheat region of the flame where temperature gradients are large (~10,000K/cm). SPIV relies on tracking the seed particles over a fixed time interval to measure the flow velocity. It is assumed that the seed particles are traveling at the same velocity as the reactant flow. SPIV is a well established and attractive tool for measuring

velocities in non-reacting flows [e.g. 60-63] because it is a non-intrusive method obtaining 3D flow velocities. SPIV and PIV have been used in combusting laminar flows [e.g. 64-69] and combusting turbulent flows [e.g. 70-73], but these flows have large thermal gradients that are not present in non-reacting flows. Seed particle velocities can lag behind the reactant flow because of thermophoretic forces.

Many studies have been done to measure the thermophoretic force in reacting flows. Experiments done in diffusion flames using LDV [43,48], in laminar counterflow flames using PIV [69], in premixed flames [73] and in stagnation flames [47,75] have all shown agreement between flame simulations and measurements that have been corrected for thermophoresis. Ref. 69 makes the thermophoretic correction in two dimensions, neglecting the out of plane component of the flamelet surface orientation. Here, results from a stationary, unstrained, planar, laminar flame calculation in a premixed methane-air flame were used to calculate estimates of the velocity difference between the particles and the reactants at the 650 K isotherm. The thermophoretic velocity correction corresponds to 2.5% of the mean reactant velocity, which is in good agreement with corrections found in Ref. 69. In turbulent flames, seed particles in the preheat region are subjected to varying strain rates caused by turbulent eddies and by thermophoretic forces. Measurements and computations reported in Ref. 75 show that the velocity difference between the reactants and the seed particles caused by thermophoresis increases with increased strain rate. Calculations reported in Ref. 69 on a one-dimensional lean laminar flame show a relatively weak sensitivity to strain rate. Thermophoretic velocity corrections that account for strain rate were not performed for the present study.

Particle velocity profiles and gas velocity profiles from the thermophoretic force calculation described above are shown in Fig. 5.5, where velocity is plotted against a spatial coordinate χ normal to the flame. These data are calculated from a

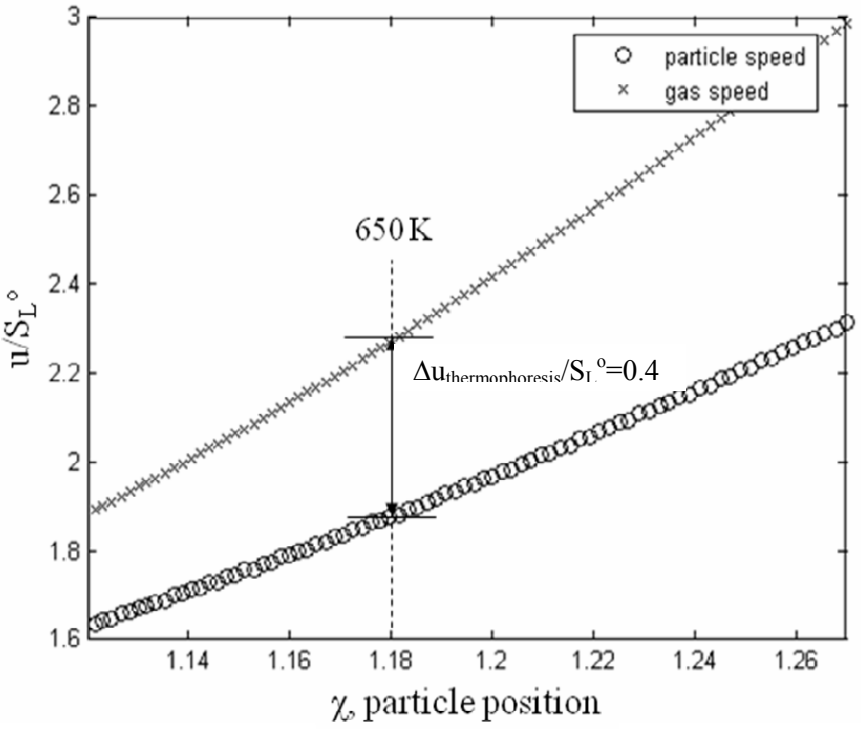

Figure 5.5: Velocity profiles from the thermophoretic force calculation of the particle and of the reactants in a lean methane-air flame. Velocity is plotted against a spatial coordinate $1.12<\chi<1.27$ (corresponding to $560<T<890$ K) normal to the flame. The values in the figure are non-dimensionalized for velocity (S^o_L) and length (α/ S^o_L, where α is the thermal diffusivity of the reactants at 650 K). These data are calculated for a stationary, unstrained, planar, laminar premixed flame model [47].

stationary, unstrained, planar, laminar premixed flame model [47] detailed in Chapter 4. Reactant and particle velocities were calculated by integrating the force balance equation (Eq. 4.12) in time, evaluating the location and velocity of the particle at each time step.

The model is in good agreement with experimental data premixed laminar counterflow flames [39, 47, 69]. The difference between the particle velocity and the reactant velocity at a specific flame location is felt to be a reasonable estimate of the difference between the seed particle velocity and reactant velocity in the present study.

After finding the particle velocities in the reactants at the 650 K isothermal surface along the two measurement lines (details above), the particle velocity component normal to the flamelet surface ($\underline{U}_p \bullet \underline{N}$) was found. In Fig. 5.5 the correction for thermophoresis that relates the particle velocity component normal to the flame to the gas velocity is shown. At the 650 K isotherm for this flame, the particle speed correction, $\Delta u_{thermophoresis}$, is 0.05 m/s. As the thermophoretic force is in the direction of decreasing temperature, the thermophoretic correction increases the reactant velocity in the direction of the normal to the flamelet surface. The reactant velocity component normal to the flamelet surface becomes:

$$\underline{U}_r \bullet \underline{N} = \left(\underline{U}_p \bullet \underline{N}\right) + \Delta u_{thermophoresis}$$

Since the measurements of $\underline{U}_r$, $\underline{N}$, and $\underline{U}_p$ are all made at the 650 K isotherm, $\Delta u_{thermophoresis} = 0.05$ m/s is the same for all of the data presented.

Flamelet Displacement Speed Results

We have extracted the particle velocity field in the SPIV image plane ($\underline{U}_p$) and the flamelet surface normal ($\underline{N}$) at points where the three-dimensional flamelet crosses the three measurement lines from 1500 image sets. Furthermore, for where the flamelet crosses the two measurement lines in the SPIV image plane we have

evaluated the velocity component of the reactants perpendicular to the flamelet surface, ($\underline{U}_r \bullet \underline{N}$), these values have been corrected for thermophoretic effects. Finally, the flamelet displacement speeds both in the laboratory reference frame (S_L) and the reference frame relative to reactants (S_L^d) were obtained from measurement of the flamelet displacement along the measurement line. Sample results are presented below to demonstrate the power of the measurement methods.

A representative velocity profile for the particles in the turbulent flame obtained from one measurement line in one image set (closed symbols) and its associated smoothed particle velocity profile (open symbols) are shown in Fig. 5.6, where velocity is plotted against a spatial coordinate along the measurement line within the SPIV mesh. The particle velocity shown is the component of the velocity vector normal to the flamelet surface, defined here as the 650 K isotherm. The particle velocity is zero where the temperature is above 650 K, the evaporation temperature of the seed particles. The velocity profile was smoothed using a moving average over 3 grid points, ~0.5 mm, that is of the order of the SPIV system registration error to reduce the contribution of measurement uncertainty in the determination of displacement speed. The observed magnitude of the fluctuations in the smoothed velocity profile is of the same order as the reactant flow turbulence intensity.

The measured reactant velocity profile was then calculated using the correction for thermophoresis, since thermophoretic forces cause a discrepancy between reactant and particle velocities in the high temperature gradient preheat region of the flame [76]. Here the thermophoretic correction was made for the first time in conjunction with the instantaneous flamelet normal in a premixed turbulent flame.

The V-flame burner used here has also been used in several previous studies in this laboratory [21, 26-27, 29, 59] and it as been shown [26-27] that the form of the PDF of $\underline{N}$ given here:

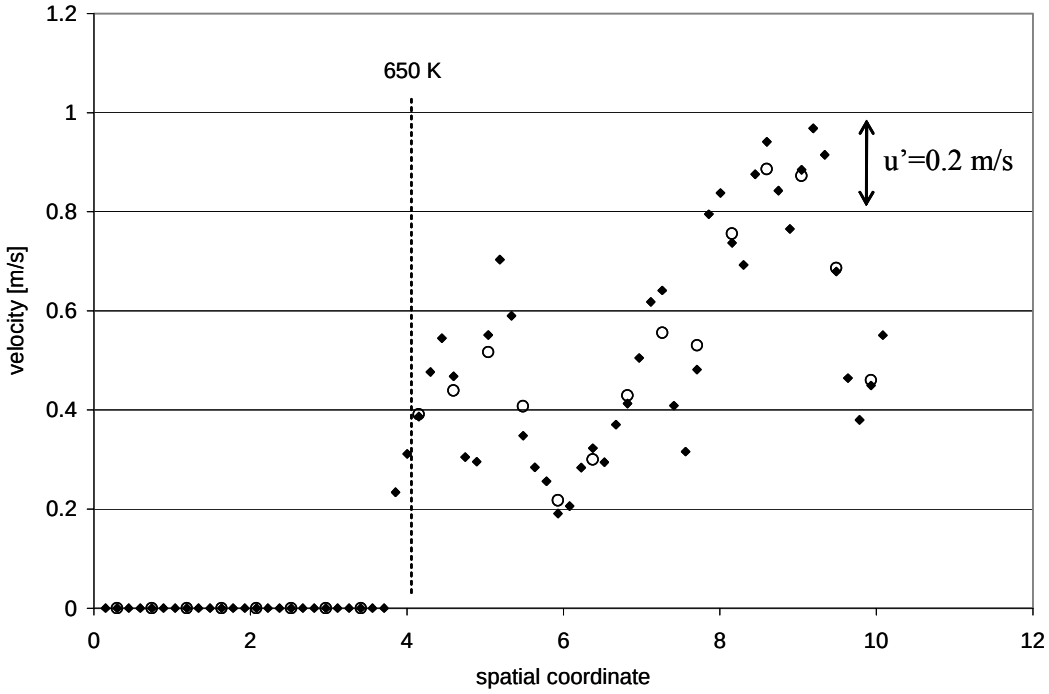

Figure 5.6: A typical instantaneous raw particle velocity profile (closed diamonds) and its average (open circles) along a measurement line. The particle velocity shown is the component of the velocity vector in the direction of the flamelet normal. The data are plotted against a spatial coordinate along the measurement line within the SPIV mesh normalized by the unstrained flame thickness. The velocity is zero where the temperature is above 650 K and no droplets exist.

$$P(\theta,\phi)d\Omega = C\exp-\left(\phi/\zeta\right)^2 \sin\phi d\phi d\theta \qquad (5.1)$$

is applicable to turbulent V-flames. For all three measurement lines in the current study, the distribution of $\underline{N}$ was determined and found to fit the form of Eq. 5.1. The distribution of flamelet orientations from crossed-plane imaging of tomography images and SPIV images (a 45° crossing angle between the image planes) is presented in the form of the marginal PDF of φ, which is shown in Fig. 5.7 for the measurement line formed by the intersection of the tomography image planes. P(φ) is formed by generating a histogram of measured φ values, independent of θ, and normalizing. The fit and data are in good agreement. Flamelet orientations were also measured with the 90° crossing angle between the two orthogonal tomography image planes. The range of the fit parameters ζ obtained from all three measurement lines is 33°≤ζ≤36° (Figs. 5.7 and 5.8). Knaus and Gouldin [27] report ζ=34° for a flame with the same value of u'/S_L^o using crossed-plane image tomography. The measured crossing-weighted [26] marginal PDF of θ for the 90° crossing angle tomography images is shown in Fig. 5.8 along with a curve of the expected marginal PDF based on the assumed PDF form; agreement between data and fit is good.

To determine the displacement speed S_L^d, it is assumed, as noted above, that the flamelet is approximately planar within the measurement volume. For the flame studied in [59] we have $\underline{N}$ data from combined crossed-plane tomography and SPIV. The conditions for that flame and experiment are similar to those of the flame studied here, except that the time between the tomography laser pulse and the first PIV laser pulse is only 64 μs – much shorter than the time delay used in the present study. The dot product of two normal vectors is a measure of the collinearity of the vectors; the closer to one the more collinear they are. From a given measurement image set, three flamelet normals are obtained. To test the collinearity of the normals in a set the dot product is taken for each possible pair of vectors from the set, giving three dot

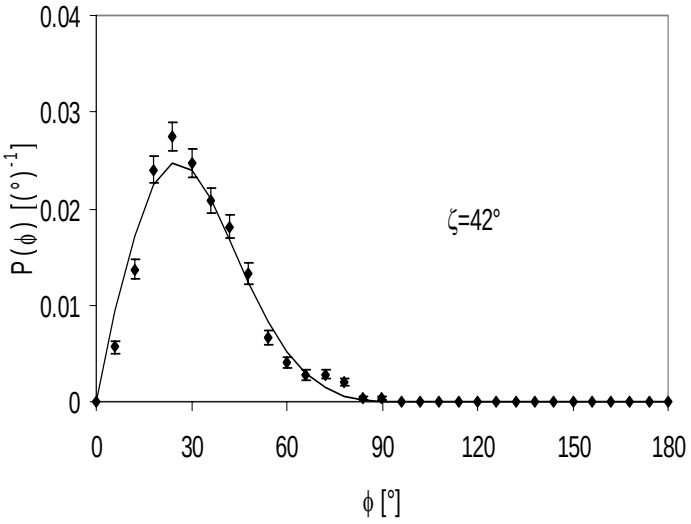

Figure 5.7: Comparison of measured PDF with assumed PDF form (curve) of polar angle angle for the measurement line from the intersecting tomography image planes. P(φ) is formed by generating a histogram of measured φ values, independent of θ, and normalizing.

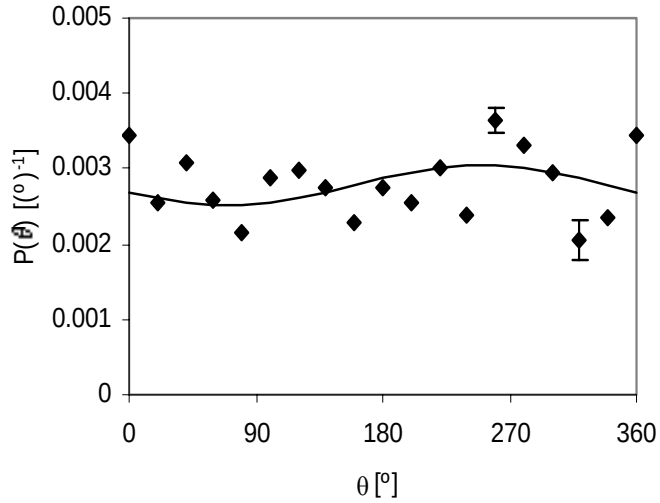

Figure 5.8: Comparison of measured PDF with assumed PDF form (curve) of the azimuthal angle, θ, for the measurement line from the intersecting tomography image planes. The measured crossing-weighted marginal PDF of θ for the 90° crossing angle tomography images is shown along with a curve of the expected marginal PDF based on the assumed PDF form.

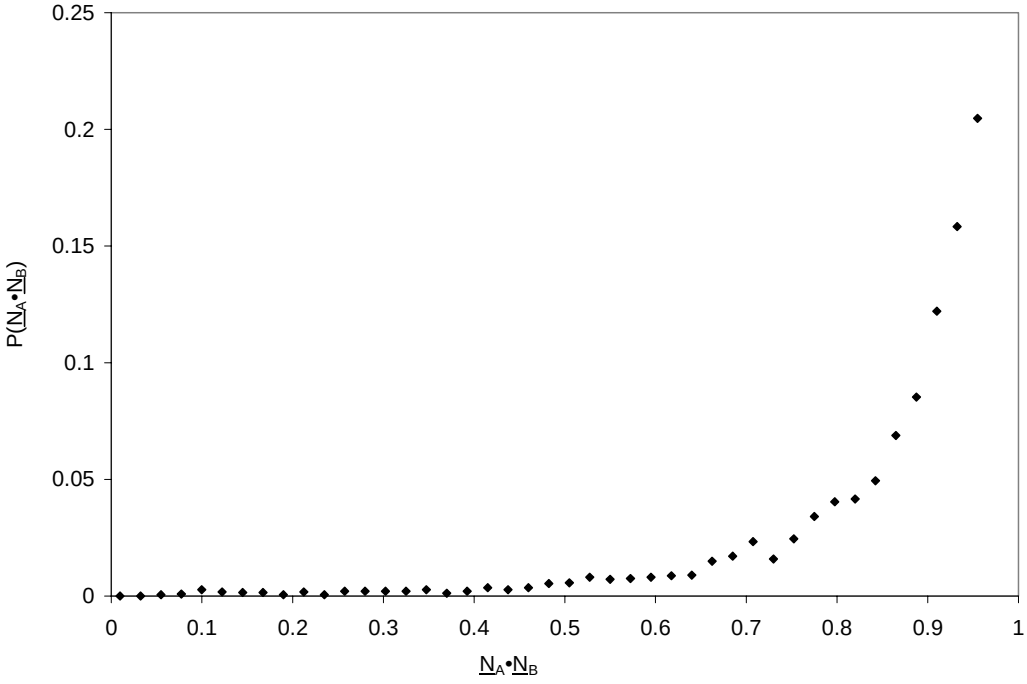

Figure 5.9: PDF of the dot product of three dimensional normal vectors along the three measurement lines.

products per set and a total of 4500 for all 1500 available image sets. The PDF of these products is shown in Fig. 5.9. It is highly peaked at 1 and therefore the result supports the assumption that the flamelet within the measurement volume is approximately planar.

The PDF of the reactant velocity component normal to the flamelet surface at the 650 K isotherm, ($\underline{U}_r \bullet \underline{N}$), is shown in Fig. 5.10. The vertical error bars in the figure indicate statistical uncertainty and are proportional to $1/(n)^{1/2}$ where n is the number of samples in each histogram bin. The horizontal error flags indicate measurement uncertainty. The generation of both the vertical and horizontal error flags will be detailed in Chapter 6. Experimental error in the SPIV system is large for small velocities (<1 m/s) and for large velocities (>2 m/s) [42]; experimental uncertainty in SPIV data ranges from 1-5%, based on test results reported in [42] of an SPIV system in which a test target consisting of hollow glass spheres suspended in a solid clear araldite block was moved on a translation stages to simulate the three dimensional motions of seed particles. Error in $\underline{N}$ depends on the CPLT measurement technique. Ref. 21 has found that error in $\underline{N}$ depend on measurement errors in φ of $\pm 0.5°$ for all φ, and on measurement errors in θ of $\pm 2.6°$ for most θ. There is also experimental error due to laser timing jitter and noise in the ICCD camera intensifiers used as electronic shutters. The horizontal error bars shown in Fig. 5.10-5.12 were estimated by the rms error given in [42] and the uncertainty analysis detailed in the next chapter. The mean of the distribution ($<\underline{U}_r \bullet \underline{N}>$) is 0.28 m/s and its standard deviation is 0.48. For comparison, we note that in a steady, unstrained laminar flame ($\underline{U}_r \bullet \underline{N}$)=$S_L^o$ where $\underline{U}_r$ is the velocity in the reactants, and for φ_{equiv} =0.65, S_L^o=0.13 m/s.

The PDF of flamelet displacement speed observed in the laboratory frame, S_L, is shown in Fig. 5.11. As before the vertical error bars indicate statistical uncertainty, while the horizontal error bars indicate measurement uncertainty in finding the

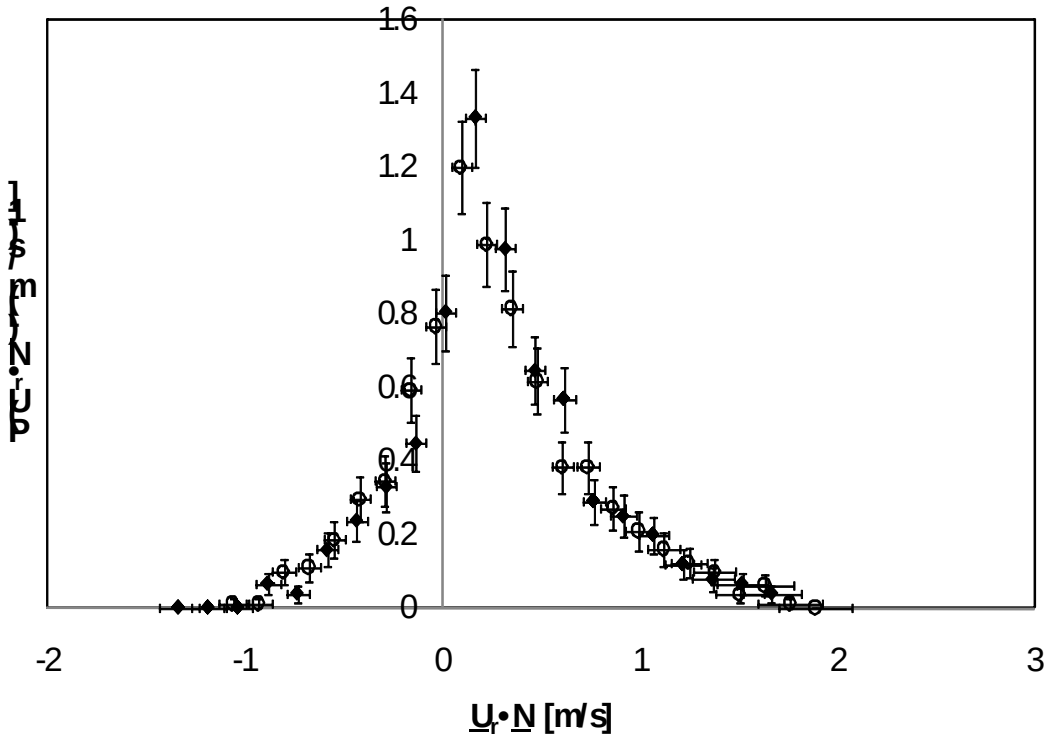

Figure 5.10: PDF of reactant velocity component normal to the reaction sheet for the two measurement lines (open and closed symbols) corrected for thermophoretic effects. The measured points are estimated from a histogram, and the vertical error flags, which indicate statistical uncertainty, are described in Chapter 6. The horizontal error flags indicate measurement uncertainty. The mean of the distribution ($\langle \underline{U}_r \bullet \underline{N} \rangle$) is 0.28 m/s and its standard deviation is 0.78.

position of the flamelet curve in each of the images. Measurement uncertainty here is also due to electronic timing jitter. Jitter in the ICCD camera intensifiers used as electronic shutters, laser pulse timing and in the SRS delay generator results in timing error both in the SPIV images used to find the particle velocity and in the timing of the tomography images used to find the flame displacement speed. The speed distribution is spread between $-2 < S_L < 2$ m/s with a mean ($<S_L>$) of -0.12±0.06 m/s and a standard deviation of 0.86.

Following the study in Ref. 54, the displacement speed is studied here in terms of the density-weighted displacement speed relative to reactants, $S_L^{d*}=\rho S_L^{d}/\rho_o$, where ρ is the fluid density at 650 K, ρ_o is the reactant density at 298 K. This density weighting was performed to minimize effects of thermal expansion. The PDF of the density weighted normalized displacement speed of the flamelet surface relative to the reactants, S_L^{d*}/S_L^{o}, measured along the two measurement lines is shown in Figure 5.12 along with error bars denoting statistical and measurement uncertainty.

It is interesting to note that this distribution has a mean near one (1.61), is broad (standard deviation=4.6), and that there is a significant probability of negative values of S_L^{d*}. The distribution has a skewness of 0.91 and a kurtosis of 3. For an unstrained laminar flame the displacement speed equals the unstretched laminar burning velocity, and one would expect that for a turbulent flame the distribution of displacement speeds would be centered around the laminar flame speed. As expected, the mean of the PDF in Figure 5.12 is 1 within experimental uncertainty. On the other hand, the breadth of the distribution and the negative values of S_L^{d*} are clear evidence of flamelet distortion by the turbulence.

Thermophoretic effects have a small but significant influence on the SPIV measurements. The effect of thermophoretic force on the raw measured reactant and flame displacement speeds is in the direction opposite the flamelet normal.

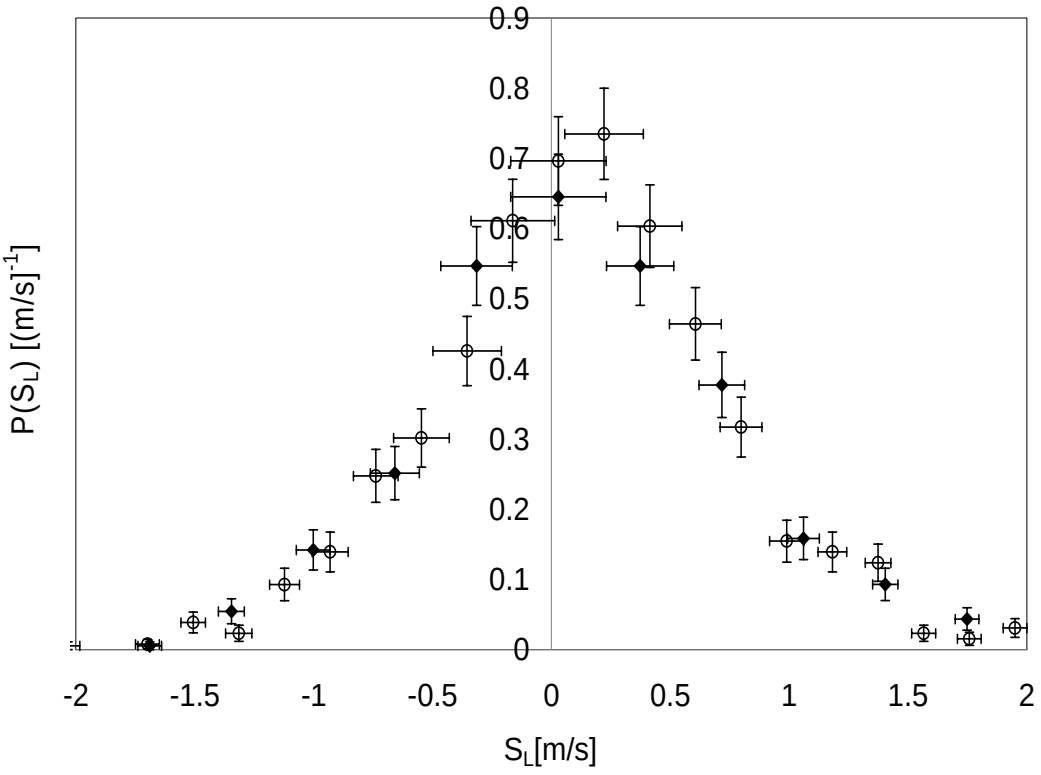

Figure 5.11: PDF of flame displacement speed in the direction of the flamelet normal, in the laboratory frame for the two measurement lines (open and closed symbols). Vertical error flags indicate statistical uncertainty due to sample size. Horizontal error flags indicate measurement uncertainty and statistical uncertainty. The mean of the distribution ($<S_L>$) is -0.03±0.06 m/s; the standard deviation is 0.70.

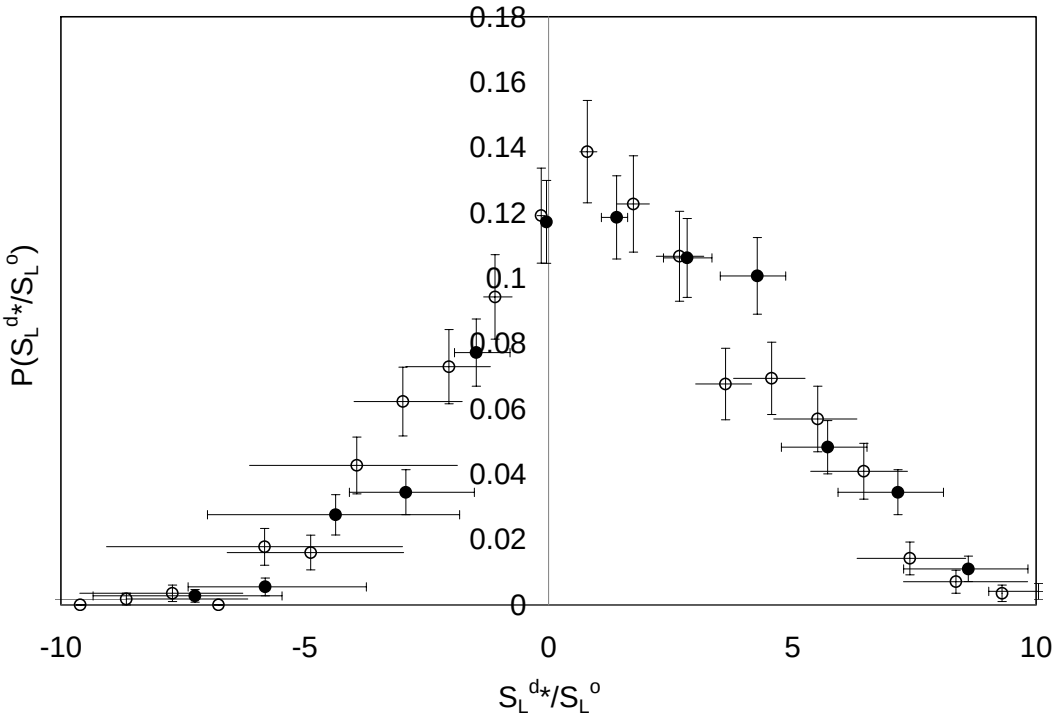

Figure 5.12: PDF of the density weighted normalized flamelet displacement speed relative to reactants and corrected for thermophoretic effects from the two measurement lines (open and closed symbols). The vertical error flags indicate statistical uncertainty and the horizontal error flags indicate measurement uncertainty. The mean of all points in the distribution ($<S_L^{d*}>/S_L^o$) is 1.61 and its standard deviation is 4.6. The most probable value is 1.1. Its skewness is 0.91 and the kurtosis is 3.04.

Unmodeled changes in the thermophoretic correction due to varying rates of strain in the turbulent flame may partially explain the breadth of the displacement speed distribution and the negative values. However, the thermophoretic velocity correction changes slowly with large increases in strain rate [69], so the breadth of the displacement speed distribution and the negative values are not entirely attributable to thermophoresis.

The uncertainty analysis detailed in the succeeding chapter was performed to understand the uncertainty in the combined CPLT and SPIV method, and to explain perhaps the negative displacement speeds in Fig. 5.12. The horizontal measurement uncertainty error flags in Fig. 5.12 show that the flags at the edges of the distribution are larger than the error flags at the center of the distribution. While large, these horizontal flags still indicate that negative flamelet displacement speeds are not likely to be the result of measurement uncertainty. The vertical error flags indicate statistical uncertainty within each bin, showing larger error at the center of the distribution compared to the error flags at the edges of the distribution. This is due to the P_{bin} term dominating Eq. 6.10 for the calculations presented here. These vertical error flags indicate that there is some error in the calculation of the height of the distribution.

While the breadth of the displacement speed PDF and the observation of negative speeds are surprising, there is supporting evidence in the literature. For example, Hisasawa, et al report displacement speeds measured in a wall-stagnating premixed flame with periodic fluctuations [38]. Variations in displacement speed are found to increase with Strouhal number to over a hundred percent. Sinibaldi et al [39, 77] report variations of displacement speed from 0.7 to 5.25 times the unstretched value in their study of two-dimensional flame-vortex interactions. DNS results of a study of a hydrogen-air triple flame subjected to an unsteady strain field [78], of a two-dimensional methane-air turbulent flame [40] and of a two-dimensional flame

interacting with a vortex [79] show large variations in displacement speeds and negative values. These studies found that displacement speeds often were negative where the strain rate was negative. While these three studies used a different isoline than that used here to define the displacement speed, we believe the results are relevant to our results. Finally, Sinibaldi et al [77] measured negative displacement speeds in methane-air premixed flames undergoing unsteady wrinkling by a laminar toroidal vortex. Negative displacement speeds were measured in the negative stretch regions of unstable flames. Sinibaldi et al [77] are unsure as to whether or not these negative values are real, and suggest that the negative values arise because of their definition of displacement speed. The displacement speed is defined here as the local flame velocity with respect to the local reactant velocity. Sinibaldi et al [77] suggest the use of another type of propagation speed, the consumption speed. The consumption speed [37] is proportional to the integral of the reaction rate per unit volume along a line normal to the flame. The consumption speed cannot become negative, but it cannot be measured with current diagnostics.

Sinibaldi et al [39] and the authors of the DNS studies [40,78-79] suggest slight modifications to steady state flame stretch theory in order to account for the S_L^d* values they observe. Flame stretch can be caused by fluid dynamic strain in the plane locally tangent to the flame and by the area change due to a curved flame propagating at a finite speed. Sinibaldi et al [77] suggested that, for their flame, only curvature changes influence the displacement speed. Refs. [77, 80-82] show a negative correlation between displacement speed and curvature for DNS studies of fully premixed flames with Lewis numbers close to 1. The joint PDF of the density weighted normalized flame displacement speed relative to reactants and two-dimensional normalized flame curvature for the two measurement lines are shown in Fig. 5.13.

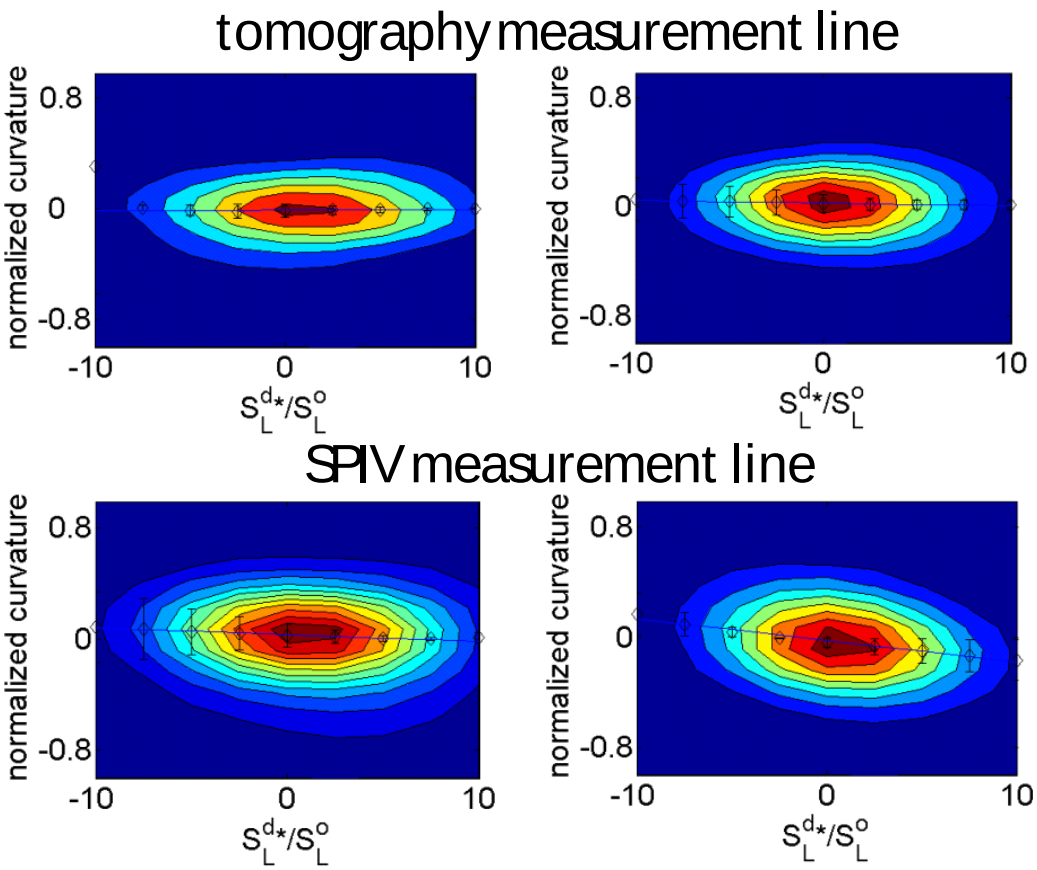

Figure 5.13: JPDF of density weighted normalized flame displacement speed relative to reactants and two-dimensional normalized flame curvature for the two measurement lines using the tomography and SPIV images. The open symbols are the maximum normalized curvature at that S_L^{d*}/S_L^o. The error flags indicate measurement and statistical uncertainty in the curvature measurements. Also indicated is the best fit line through these calculated maxima.

Flame curvature is measured in both of the tomography images. Where the flamelet boundary intersects the measurement line in both images, the boundary is locally fit with a third-order polynomial, using a fit width of 80 pixels (6 mm, determined by observing the resulting fits for different fit widths of the flamelet boundary in unprocessed images). For each image set the two-dimensional flamelet curvature is measured for the two measurement lines. The data set was then analyzed to find the joint PDF of curvature with S_L^{d*}/S_L^{o}. The JPDF surface is estimated by generating a three-dimensional histogram, where the data are smoothed using a symmetric Gaussian lowpass filter of size [3 3] with a sigma of 0.95, and normalizing. The open symbols in the plots are the maximum normalized curvature at that S_d^{*}/S_L^{o}. The vertical error flags indicate measurement and statistical uncertainty in the curvature measurements. Also indicated is the best fit line through these calculated maxima. As shown in Fig. 5.13, there is a weak correlation of negative displacement speeds to large positive flamelet curvature and thus to distortion of the preheat zone. The results found in Sinibaldi's [39,77] flame-vortex study and the trends found in the DNS studies [40,76-77, 80-83] found strong correlations in negative displacement speeds with large positive curvatures for more turbulent flames. The curvature measured here is the two-dimensional curvature in the two tomography image planes. The curvatures measured in [39-40, 77-83] are the principal curvatures of the flamelet surface. To further investigate the causes of these measured displacement speeds, the three-dimensional curvature of the flamelet surface should be measured.

CHAPTER 6

UNCERTAINTY ASSESSMENT OF THE FLAMELET DISPLACEMENT SPEED MEASUREMENT METHOD

The combined crossed-plane laser tomography and stereo PIV method was used to measure $\underline{U}_r$, S_L, $\underline{N}$, and the normalized, density-weighted displacement speed S_L^{d*}/S_L^{o} for each of the 1500 image sets taken for this flame. The PDFs of $\underline{U}_r$, S_L, $\underline{N}$, and S_L^{d*}/S_L^{o} are presented in Figs. 5.7, 5.10-5.12. $\underline{U}_r$ was evaluated from measurements of particle velocity and from calculations of the thermophoretic force correction, S_L was obtained from measurements of the flamelet displacement along the measurement line, $\underline{N}$ was found from simultaneous orthogonal single plane imaging measurements, and S_L^{d*}/S_L^{o} is defined here as a function of $\underline{U}_r$, S_L and $\underline{N}$:

$$S_L^{d*} / S_L^{o} = \left(\underline{U}_r - S_L \underline{N}\right) \bullet \underline{N} \frac{\rho}{\rho_o S_L^{o}} \tag{6.1}$$

where ρ is the product density, ρ_o the reactant density and S_L^{o} is the unstretched laminar flame speed. Each of the individual measurements (i.e. particle velocity, the location of the flame boundary) is a source of error. These errors propagate to the calculated quantities $\underline{U}_r$, S_L, $\underline{N}$, and S_L^{d*}/S_L^{o} as measurement uncertainty and are indicated by the horizontal error flags in Figs. 5.10-5.12. The vertical error flags in these figures indicate statistical uncertainty due to sample size. This chapter will first discuss the individual sources of error associated with the combined CPLT and SPIV measurement method, then give a description of how these errors propagate to $\underline{U}_r$, S_L, $\underline{N}$, and S_L^{d*}/S_L^{o}, and finally describe how the statistical uncertainty and the calculated measurement uncertainty in the individual realizations of $\underline{U}_r$, S_L, $\underline{N}$, and S_L^{d*}/S_L^{o} are represented in the PDFs of these values.

The combined crossed-plane laser tomography and stereo PIV method is

subject to four types of measurement error: (1) instrumentation errors, i.e.: error due to system setup and image processing, (2) uncertainty in the crossed-plane laser tomography measurement technique, (3) uncertainty in the SPIV measurement technique, and (4) uncertainty in the thermophoretic velocity correction. The individual sources of error that fall into each of these categories are discussed in detail below.

Instrumentation Errors

Flamelet displacement speed measurements were performed on the V-flame burner system used in several pervious studies in this laboratory [21, 26-27, 29, 59]. Fuel (commercial grade methane) and air flows were controlled by mass flow meters and premixed in a plenum at the base of the burner. The calibration of the fuel mass flow meter was performed with air and corrected for the fuel metering conditions, and is accurate to within ±3.0% [31]. The estimated calibration accuracy of the air mass flow meter is ±0.5% of the mass flow rate [31]. The resulting uncertainty in equivalence ratio is ±0.02. The uncertainty in the equivalence ratio results in an uncertainty in calculating the unstretched flame speed, S_L^o, of ±0.02 m/s [85] and in determining the reactant density ratio, ρ/ρ_o, of ± 0.012.

There are several sources of random error arising from the combined CPLT and SPIV experimental setup. Error is caused by time jitter in the ICCD camera intensifiers used as electronic shutters and in the laser pulse timing, which results in timing errors. These errors were determined to be approximately ±1 μs for the cameras, lasers and SRS electronic delay generator [29, 56] which are small compared to both the CPLT and SPIV pulse delay of 1.5 ms but are included in the uncertainty analysis here.

There is also uncertainty in the location of the field of view of all 6 cameras.

These errors were minimized through use of a transparent optical alignment target. The alignment target was placed in the field of view of all cameras. The resulting uncertainty, determined from the resolution of the target by the cameras, is approximately ±0.2 mm.

There is random error caused by image resolution and image processing in the determination of the location of the flame boundary in both the CPLT and the SPIV images. Uncertainty in the determination of the location of the intersection of the flame boundary with the measurement line is caused by the discrete nature of the oil droplets. Uncertainty due to the image resolution is small compared to the uncertainty due to the discrete droplets identified in the images. The influence of the random error due is minimized through curve fitting both the measurement line and the flame boundary in the image. This error can be estimated based on the uncertainties in the least squares, third order polynomial fit parameters of the curve fits, which are a reflection of the agreement of the fits with the flamelet boundary data. A third order polynomial fit was chosen based on visual inspection, that showed a third order polynomial fit matched the flamelet boundary data well. Based on the measured uncertainties of the goodness of the least squares fits, the uncertainty in determination of the location of the flame boundary in the CPLT and SPIV images is ±0.2 mm, which is in agreement with previous CPLT measurements, Ref. [21,29].

Uncertainty in the crossed-plane tomography measurement technique

Uncertainty in $\underline{N}$ depends on the CPLT measurement technique, and was analyzed in detail in Knaus et al [21]. Knaus et al analyzed a test image of a perturbed laminar V-flame, to determine the error in the flamelet normal determination at different locations along the flamelet boundary. They found that when $\underline{N}$ is expressed in terms of a spherical coordinate system, with φ the polar angle and θ the azimuthal

angle with respect to a polar axis aligned with the mean orientation $\langle \underline{N} \rangle$, there was an error in φ with an average value of ±0.5° for all φ, and an error in θ with an average value of ±2.6°. Random error in the measurement of $\underline{N}$ resulted from several sources: uncertainty in the location of the measurement line, error in the angle between the laser sheets, and finite laser sheet thickness. Uncertainty in the location of the measurement line in each image results in tangents not being evaluated at the same location on the flamelet surface. This error is significant near cusps, where small error in the determination of the measurement line can result in large errors in slope. Uncertainty in the location of the measurement line is limited by the finite thickness of the laser sheet. To reduce the error in determining the measurement line in this experiment, an algorithm for a linear least square fit was used to find the line of intersection between the laser sheets. Error analysis based on the linear least squares fit used here to find the measurement line indicates that the uncertainty in the location of the line is ±0.2 mm.

The angles between the laser sheets were also measured, and were within ±2% of their reported value. Ref. [21] also performed a simulation to randomly generate surface normals in a vertical plane. The angles of the laser sheets with respect to the vertical were varied in order to study the effect on measurement error of error in laser sheet alignment. If one sheet is at 49° and the other at 45°, a 9% error in laser sheet alignment, the average error in φ is 0.25°, while the error in θ is 2.0°. This small amount of error in φ and θ for a 9% error in the angle between the laser sheets demonstrates that there is little error introduced into the $\underline{N}$ measurement due to error in laser sheet angle.

Uncertainty in the SPIV measurement technique

The $\underline{U}_r$ measurement depends on the measurement of $\underline{U}_p$, the instantaneous

three-dimensional velocity of the seed particles, $\underline{N}$ (discussed above), and the correction for thermophoretic force effects. The accuracy of the SPIV system was investigated by performing SPIV measurements on a test target consisting of hollow glass spheres suspended in a solid clear araldite block [42]. The target was moved on translation stages to simulate the three dimensional motions of the seed particles. The error in $\underline{U}_p$ is found to be large for small velocities (< 1 m/s) and for very large velocities (> 2 m/s). In the test results presented in Ref. [42], error in $\underline{U}_p$ for values between 1 and 2 m/s was ±1% while error in $\underline{U}_p$ outside of this range was found to be ±5%.

There is also concern regarding the accuracy of $\underline{U}_p$ when the SPIV measurement method is applied to a flame, where there are refractive index changes. The average particle displacement in this study is ~1 mm for a SPIV interpulse time of 42 μs. The light from both images arrives at the camera with very little separation in time. Ref. [43] shows that the resulting exposures are influenced by very similar refractive index gradients such that refractive index fluctuations are unimportant.

Uncertainty in the thermophoretic correction

When SPIV measurements are performed near the flame, the effects of thermophoresis must be considered. For the micron sized silicone oil droplets used in this study, the thermophoretic velocity has been calculated for a stationary, unstrained planar laminar premixed lean (φ_{equiv}=0.65) methane-air flame. An estimate of the thermophoretic force and SPIV particle velocity relative to the gas phase was calculated. In accordance with the experiment, the flame-front location was assumed to be determined by the position of the 650 K isotherm in the calculation. Computations for this lean flame predict that the particle velocity lags behind the gas velocity by $\Delta u_{thermophoretic}/S_L^o$=0.4, which is 2.5% of the mean reactant flow velocity.

The direction of the thermophoretic force is normal to the flame front and towards the reactants. This correction is in good agreement with thermophoretic effects measured in [69], which found that the thermophoretic velocity correction could range from 1-3% of the mean reactant velocity.

Because this correction was based on a premixed lean (φ_{equiv}=0.65) flame at the 650 K isotherm, there is uncertainty when $\Delta u_{thermophoretic}/S_L^o$ is applied to the current experiment, where the equivalence ratio and measurement isotherm are known only to within uncertainties. For the flame studied here there is an error in air and fuel flow rates, which results in an uncertainty in φ_{equiv}, and an error in determining the location of the flame boundary, which results in uncertainty in the location of the 650 K isotherm. Computations were performed for a range of lean flames (φ_{equiv}=0.65±0.02), and the thermophoretic velocity correction was evaluated for locations within 0.2 mm of the 650 K isotherm, i.e. within the uncertainty of determining the flamelet boundary location. The thermophoretic velocity correction was found for each flame at each isotherm location. These computations indicated an uncertainty in the thermophoretic velocity correction of ±3%.

Calculation of uncertainty in flamelet displacement speed

Each of the individual sources of error detailed above affect the calculated uncertainty of $\underline{N}$, $\underline{U}_r$, S_L, and $S_L^d{}^*/S_L^o$. For each of these quantities, Table 6.1 lists the relevant individual sources of error. The calculated uncertainty of $\underline{N}$ depends on the accuracy of the measurement of the polar angle φ and the azimuthal angle θ, the uncertainty of the location of the measurement line, and uncertainty in the angle between the laser sheets. The calculated uncertainty of $\underline{U}_r$ depends on the accuracy of the measurement of the seed particle velocity $\underline{U}_p$, the uncertainty in the thermophoretic

velocity correction[2] and the calculated uncertainty of $\underline{N}$. The calculated uncertainty of S_L depends on camera and laser jitter, camera registration error, uncertainty in the location of the flamelet boundary and the calculated uncertainty of $\underline{N}$. The calculated uncertainty of S_L^{d*}/S_L^{o} depends on the calculated uncertainty of $\underline{U}_r$, $\underline{N}$, S_L, ρ/ρ_o, and S_L^{o} (Eq. 6.1). The propagation of error from a single measurement to a calculated quantity such as $\underline{U}_r$, $\underline{N}$, S_L, and S_L^{d*}/S_L^{o} has been discussed by Bevington [86]. The procedure detailed in Ref. [86] is followed here.

To see how error propagates from a measured value to a calculated quantity, consider a general quantity x which could represent $\underline{U}_r$, $\underline{N}$, S_L, or S_L^{d*}/S_L^{o}. x is a function of a set of general measured variables u, v, etc., where u and v could be $\underline{U}_p$ and the location of the flamelet boundary:

$$x = f(u, v, ...) \tag{6.2}$$

The effect of uncertainty on the function x can be found by considering the spread of the values of x which result from combining the measurements from individual realizations, u_i, v_i, w_i, etc. into individual results x_i, where i represents the i^{th} realization in our set of 1500 measurements:

$$x_i = f(u_i, v_i, ...) \tag{6.3}$$

Following Bevington [86], assume that the mean value of x is:

$$\bar{x} = f(\bar{u}, \bar{v}, ...) \tag{6.4}$$

where the overbar indicates a mean quantity. For an infinite number of measurements, the mean of the distribution of x will coincide with the average and the variance can be expressed as

$$\sigma_x^2 = \lim_{N\to\infty} \frac{1}{N} \sum_i^N \left(x_i - \bar{x}\right)^2. \tag{6.5}$$

[2] The thermophoretic velocity correction is treated here as an independent variable, although it actually depends on equivalence ratio and on the location of the flamelet boundary. However, the effect of this correlation is negligibly small: when error bars were recalculated with explicit dependence on equivalence ration and flamelet boundary location, the correction was on the order of 0.2%.

The uncertainty in x for an individual realization goes as

$$x_i - \bar{x} \cong \left(u_i - \bar{u}\right)\left(\frac{\partial x}{\partial u}\right) + \left(v_i - \bar{v}\right)\left(\frac{\partial x}{\partial v}\right) + \cdots \tag{6.6}$$

where each of the partial derivatives is evaluated with all other variables fixed at their mean values. Substituting Eq. 6.6 into Eq. 6.5 gives

$$\begin{aligned}\sigma_x^2 &\cong \lim_{N\to\infty}\frac{1}{N}\sum\left[\left(u_i - \bar{u}\right)\left(\frac{\partial x}{\partial u}\right) + \left(v_i - \bar{v}\right)\left(\frac{\partial x}{\partial v}\right) + \cdots\right]^2 \\ &\cong \lim_{N\to\infty}\frac{1}{N}\sum\left[\left(u_i - \bar{u}\right)^2\left(\frac{\partial x}{\partial u}\right)^2 + \left(v_i - \bar{v}\right)^2\left(\frac{\partial x}{\partial v}\right)^2 + 2\left(u_i - \bar{u}\right)\left(v_i - \bar{v}\right)\left(\frac{\partial x}{\partial u}\right)\left(\frac{\partial x}{\partial v}\right) + \cdots\right]\end{aligned} \tag{6.7}$$

An approximation of Eq. 6.7 would be

$$\sigma_x{}^2 \cong \sigma_u{}^2\left(\frac{\partial x}{\partial u}\right)^2 + \sigma_v{}^2\left(\frac{\partial x}{\partial v}\right)^2 + 2\sigma_{uv}{}^2\left(\frac{\partial x}{\partial u}\right)\left(\frac{\partial x}{\partial v}\right) + \cdots \tag{6.8}$$

The first two terms in Eq. 6.8 are averages of the squares of the deviations, which dominate σ_x^2. The third term in Eq. 6.8 is the average of the cross terms involving products of deviations in u and v simultaneously. σ_{uv} is the estimated covariance between the u and v measurements. This term is only important if u and v are correlated. Here we assume that u and v are not correlated and Eq. 6.8 reduces to

$$\sigma_x{}^2 \cong \sigma_u{}^2\left(\frac{\partial x}{\partial u}\right)^2 + \sigma_v{}^2\left(\frac{\partial x}{\partial v}\right)^2 + \cdots \tag{6.9}$$

Eq. 6.9 was used here to calculate the uncertainty in $\underline{U}_r$, $\underline{N}$, S_L, and $S_L{}^{d*}/S_L{}^{o}$. $\underline{U}_r$, $\underline{N}$, S_L, and $S_L{}^{d*}/S_L{}^{o}$ were written as functions of their measured values. An algorithm was written to determine the uncertainty of these quantities from the uncertainty for each individual measurement in accordance with Eq. 6.9. The individual measurements that are used to determine $\underline{U}_r$, $\underline{N}$, S_L, ρ/ρ_o, and $S_L{}^{o}$ have been discussed above and are summarized in Table 6.1.

Table 6.1: Summary of measured uncertainties used in determining the values $\underline{N}$, $\underline{U_r}$, S_L, S_L^o, and ρ/ρ_o, and the uncertainties of the measured quantities.
Note: The starred values represent quantities that were not measured directly. The thermophoretic velocity correction was determined from the location of the flamelet boundary and the equivalence ratio, which in turn was determined from the fuel and air flow rates.

Measurement	Units	Error
$\underline{N}$		
• φ, polar angle	degrees	0.5
• θ, azimuthal angle	degrees	2.6
• Measurement line location	mm	0.2
• Angle between laser sheets		2%
$\underline{U}$r		
• $\underline{N}$		
• $\underline{U_p}$	-	1% 1>$\underline{U_p}$>2 m/s, 5% otherwise
• Thermophoretic velocity correction*	-	3%
S_L		
• Camera and laser jitter	μs	1
• Camera registration error	mm	0.2
• Location of flame boundary	mm	0.2
• $\underline{N}$		
S_L^o		
• Equivalence ratio*	-	0.02
ρ/ρ_o		
• Equivalence ratio*	-	0.02

The algorithm was used to determine the uncertainty of $\underline{U}_r$, $\underline{N}$, S_L, and S_L^{d*}/S_L^{o} for each realization i from the uncertainty for each individual measurement listed in Table 6.1. This experiment produced 1500 image sets. The algorithm calculated 1500 values of $\underline{U}_r$, $\underline{N}$, S_L, and S_L^{d*}/S_L^{o} and the uncertainties associated with each value.

The calculated results are presented here as PDFs of $\underline{U}_r$, $\underline{N}$, S_L, and S_L^{d*}/S_L^{o}, Figs. 5.7 and 5.10-5.12. The PDFs were formed by generating a histogram of the calculated results and normalizing. However, each value of $\underline{U}_r$, S_L, $\underline{N}$, and S_L^{d*}/S_L^{o} has a calculated uncertainty. The following describes how the calculated uncertainty in the individual values of $\underline{U}_r$, S_L, $\underline{N}$, and S_L^{d*}/S_L^{o} are represented in the PDFs.

Consider the PDF of S_L^{d*}/S_L^{o}. Each realization $(S_L^{d*}/S_L^{o})_i$ has an associated calculated uncertainty $\delta(S_L^{d*}/S_L^{o})_i$. Within each histogram bin, the uncertainty $\delta(S_L^{d*}/S_L^{o})_i$ was used to compute the probability that a point with mean $(S_L^{d*}/S_L^{o})_i$ and error $\delta(S_L^{d*}/S_L^{o})_i$ should fall into that bin [87]. This was done by integrating a Normal distribution with mean $(S_L^{d*}/S_L^{o})_i$ and standard deviation $\delta(S_L^{d*}/S_L^{o})_i$ over the range of the histogram bin. Each data point $(S_L^{d*}/S_L^{o})_i$ in the histogram bin now has a probability P_i of being in that bin. The calculated measurement uncertainty of the center value of a given histogram bin [87] is then given by:

$$\left(\sum_{1}^{Nbin} P_i \delta(S_L^{d*} / S_L^{o})_i \right) / \sum_{1}^{Nbin} P_i \tag{6.9}$$

where Nbin is the number of data points $(S_L^{d*}/S_L^{o})_i$ within that histogram bin. This data analysis procedure was applied to $\underline{U}_r \bullet \underline{N}$, S_L and S_L^{d*}/S_L^{o} data to provide the horizontal error flags in Figs. 5.10-5.12.

The vertical error flags in Figs. 5.7, 5.10-5.12 denote statistical uncertainty due to sample size. The statistical uncertainty of a given histogram bin [29] is

$$\frac{P_{bin}}{(P_{bin} bwN)^{1/2}} = \left(\frac{P_{bin}}{bwN} \right)^{1/2} \tag{6.10}$$

where P_{bin} is the value of the PDF at that bin, bw is the bin width and N is the total number of samples in the entire distribution.

CHAPTER 7

SUMMARY

This work is the continuation of a series of experiments in this laboratory to gather three-dimensional information about the wrinkling of flamelet surfaces via crossed-plane laser tomography (CPLT). Information on the level of wrinkling in turbulent flames is important because in premixed turbulent combustion in the flamelet regime, the reaction rate of a flame is proportional to the amount of flamelet surface area per unit volume. A major effect of turbulence is to wrinkle the flamelet, increasing the flamelet surface area and thus the reaction rate. When the author started working in this laboratory, the CPLT technique was considered valid: its uncertainty had been assessed, and the technique applied to the study of both turbulent V-flames and SI engine flames. From these studies it was found that the form of the distribution of flamelet orientations $\underline{N}$ is universal – it is quasi-Gaussian; it is independent of the azimuthal direction; and it depends only on a single parameter, ζ. The CPLT technique was used in this work with other imaging techniques to further investigate the wrinkling of flamelet surfaces and the internal structure of the flamelet.

The CPLT technique was first used to measure in-plane flamelet curvature in laboratory V-flames. Taking advantage of the simple universal form of the PDF of $\underline{N}$ and its dependence on ζ, it was shown that ζ can be determined from two-dimensional image data provided that the image plane is aligned correctly. If the image plane is aligned perpendicular to <c> constant surfaces, the universal form of the PDF of $\underline{N}$ holds. ζ and A_T/A, the mean flamelet area increase due to turbulence, were measured from two-dimensional image data and are found to grow linearly with distance from the V-flame stabilizing rod. The observed growth rates in ζ and A_T/A vary considerably from flame to flame, and the differences cannot be explained solely by

changes in u'/S_L^o, the ratio of the turbulence intensity to the unstretched laminar flame speed. This result suggests that local burning rates in wake flames, e.g., bluff body-stabilized flames, vary with downstream distance and cannot be quantified by a single number. It is possible that this variation from flame to flame is due to mean flow suppression of surface production, i.e. stretch effects.

The CPLT technique was also used in combination with stereo PIV (SPIV) to simultaneously measure three-dimensional flamelet orientation and three-dimensional reactant velocity. This combined technique measured instantaneous flamelet surface curvature and the flamelet displacement speed, defined as the component of the relative velocity between the reactants and the flame surface that is normal to the surface. The displacement speed is an important measure of unsteady stretched laminar flames and turbulent flames. Previous workers [37-38] have suggested that the displacement speed is a function of Markstein and Karlovitz numbers and is a measure of the combined effects on flamelets of strain and unsteadiness in turbulent flames. Displacement speed measurements in premixed turbulent flames are difficult and prior to this work have not been done because they require the simultaneous measurement of reactant velocity, flamelet speed in the laboratory frame and the flamelet surface orientation. By combining crossed-plane tomography and stereo particle image velocimetry (SPIV) and staggering in time the tomography and SPIV laser pulses we are able to measure all three of these quantities. What is presented here is the first instantaneous measurement of the three-dimensional flamelet displacement speed.

SPIV as applied here measures the seed particle velocity in the reactants. In SPIV, three-dimensional velocity measurements are obtained using two cameras. Each camera records an image pair separated by a short time interval and views the same region of the flame from a different perspective. Based on these different views

of particle displacements the out of plane of velocity is determined. The accuracy of SPIV to measure the reactant velocity depends on how closely the seed particles follow the flow. It is often assumed that the seed particles are traveling at the same velocity as the reactant flow. However, seed particle velocities can lag behind the reactant flow because of thermophoretic forces in regions of high temperature gradients. Here, results from a stationary, unstrained, planar, laminar flame calculation were used to calculate estimates of the velocity lag due to thermophoresis of the particles in the reactant flow. The thermophoretic velocity correction is in good agreement with corrections found in other studies [69] of flat flames. The thermophoretic force correction was used here in combination with flamelet surface orientation data for the first time. Since the thermophoretic force is in the direction of decreasing temperature, all three coordinates of flamelet surface orientation must be considered when applying the velocity correction. In turbulent flames, seed particles in the preheat region are also subjected to varying strain rates caused by turbulent eddies in addition to thermophoretic forces. Measurements and computations [75] show that the velocity difference between the reactants and the seed particles caused by thermophoresis increases with increased strain rate. Thermophoretic velocity corrections that account for strain rate were not performed for the present study.

The combined crossed-plane laser tomography and stereo particle image velocimetry (SPIV) method is applied to measure three-dimensional flamelet orientation, reactant velocity, and flamelet displacement along a measurement line in premixed turbulent flames. From these data, the velocity components (corrected for thermophoresis) of the reactants perpendicular to the flamelet surface are determined. The flamelet displacement speed is obtained from the measurements of flamelet displacement and reactant velocity at the flamelet surface. Flamelet displacement speed data show both a broad distribution of values and a significant probability of

negative values. The breadth of the distribution and the presence of negative displacement speeds are attributed to high values of curvature and extensive tangential strain. While the breadth of the displacement speed PDF and the observation of negative speeds are surprising, there is supporting evidence in the literature. Measurements made in Refs. [38-39, 77] have also found negative displacement speeds and a large variation of values. DNS studies [40,78-79] show large variations in displacement speeds and negative values. These studies found that displacement speeds often were negative where the strain rate was negative. It was found here that there is a weak correlation of negative displacement speeds to large positive flamelet curvature, however the curvature measured is the two-dimensional curvature in the tomography image plane.

The uncertainty in the combined crossed-plane tomography and stereo particle image velocimetry method was assessed, and the uncertainty of the measured flamelet displacement speed was calculated. Since the flamelet displacement speed is not measured directly (it is determined from several measured quantities in the combined method), errors from individual measurements propagate to the displacement speed. The errors from the individual measurements were identified and a propagation of error analysis was performed to calculate the uncertainty in the flamelet displacement speed results. Large measurement uncertainty was found at the edges of the displacement speed distribution compared to the measurement uncertainty at the center of the distribution. While this indicates that there is significant measurement uncertainty associated with the negative displacement speed values, the uncertainty estimates indicate that negative values are real and are not the result of measurement uncertainty.

This work has discussed the development of a new technique, combined crossed-plane laser tomography with stereo PIV. This technique was used to measure

for the first time the instantaneous flamelet displacement speed. The combined technique was demonstrated on a premixed turbulent flame and its uncertainty was assessed. The flamelet displacement speed results are surprising, the distribution of displacement speeds measured is broad and shows evidence of the existence of negative displacement speeds. While both negative displacement speeds and a large range of displacement speeds have been seen in the literature [38-40, 75-77], the negative displacement speeds were found in highly turbulent flames. The flame studied here has a relatively weak turbulence intensity when compared to the flames studied in the literature. The measured displacement speeds in the literature use in-image plane flamelet orientation to correct the seeded flow for thermophoresis, neglecting the out of plane component and thus inaccurately implementing the thermophoretic force correction. The results presented here is the first body of data of the instantaneous, directly measured flamelet displacement speed. The thermophoretic correction was applied to seeded flows in combination with measured three-dimensional flamelet orientation data for the first time. These measurements have laid the groundwork for future studies measuring displacement speeds using the combined crossed plane laser tomography and stereo PIV technique.

In closing, the author would like to propose ideas to further extend this work. The universal form of the distribution of flamelet orientations is valuable and makes it possible to measure three-dimensional flamelet orientation easily. This method should be applied to more flames in addition to the turbulent V-flames studied here. It is possible that the rod wake influenced some of the results presented here. Other burners should be studied in addition to a wider range of turbulent flames and reactant mixtures to study how ζ and A_T/A grow with distance downstream from the flame stabilizer. Growth rates of ζ and A_T/A are widely considered to be a function of u'/S^o_L, and it has been suggested here that there may be other factors needed to explain

observed growth.

The combined CPLT and stereo PIV technique should also be applied to more flames that fall within the thin reaction zone regime of premixed turbulent combustion where large distortions of flamelet structure are expected. Also steps need to be taken to measure the third component of flamelet curvature. This combined measurement technique is very powerful and can provide much needed insight into the effect of turbulence on the structure of the preheat zone of the flamelet.

REFERENCES

1. DOE website: www.energy.gov/energysources/fossilfuels.htm July 2007.

2. The White House Office of Communications, "Twenty in Ten: Strengthening America's Energy Security" (2007).

3. Barlow, R.S., Proc. Combust. Inst. 31:49-75 (2007).

4. Peters, N. Turbulent Combustion, Cambridge, UK: Cambridge University Press (2000).

5. Sivashinsky, G.I., Proc. Combust. Inst. 29:1737-1761 (2002).

6. Veynante, D. and Vervisch, L., Prog. Energy Combust. Sci., 28:193-266 (2002).

7. Bray, K.N.C., Libby, P.A., Masuya, G., et al. Combust. Sci. Technol. 25:127 (1981).

8. Bray, K.N.C., Libby, P.A., and Moss, J.B., Combust. Flame 61:97 (1985).

9. Bray, K.N.C., Champion, M., and Libby, P.A., Combust. Sci. Technol. 55:139 (1987).

10. Cant, R.S., and Bray, K.N.C. Combust. Flame 76:243 (1989).

11. Libby, P.A. Prog. in Energy and Combust. Sci. 11:83 (1985).

12. Bray, K.N.C. and Peters, N. Turbulent Reacting Flows (P.A. Libby and F.A. Williams eds.) Academic Press, San Diego, 1984.

13. Gouldin, F.C. Proc. Combust. Inst. 26:381-388 (1996).

14. Cant, R.S., Pope, S.B., Bray, K.N.C. Proc. Combust. Inst. 23:809-815 (1990).

15. Borghi, R. Combust. Flame 80:304 (1990).

16. Darabiha, N., Giovangili, V., Trouve, A., et al, Turbulent Reacting Flows, Springer-Verlag, New York 1989.

17. Poinsot, T. Proc. Combust. Inst. 26:219-232 (1996).

18. Shepherd, I.G., and Ashurst, W.T. Proc. Combust. Inst. 24:485-491 (1992).

19. Bray, K.N.C, Libby, P.A., and Moss, J.B., Combust. Sci. Tech. 41:143-172 (1984).

20. Gouldin, F.C., Physical and Cemical Aspects of Combustion: A Tribute to Irvin Glassman, Gordon and Breach, Amsterdam, The Netherlands, p. 433 (1997).

21. Knaus, D.A., Gouldin, F.C., and Bingham, D.C., Combust. Sci. Technol. 174:101-134 (2001).

22. Lee, T.-W., North, G.L., Santavicca, D.A. Combust. Sci. Technol. 84:121 (1992).

23. Lee, T.-W., North, G.L., Santavicca, D.A. Combust. Flame 93:445-456 (1993).

24. Smallwood, G.J., Deschamps, B.M. SAE Paper 962088 (1996).

25. Bingham, D.C., M.S. thesis, Cornell University, 1998.

26. Bingham, D. C., Gouldin, F. C., and Knaus, D. A., Proc. Combust. Inst. **27**: 77-84 (1998).

27. Knaus, D. A., and Gouldin, F. C., Proc. Combust. Inst. **28**:367-373 (2000).

28. Knaus, D. A., Gouldin, F. C., Hinze, P. C., and Miles, P. C., *SAE Trans.* **108**, paper no. 1999-01-3543 (1999).

29. Knaus, D.A., Ph.D. Diss., Cornell University, 2003.

30. Boyer, L., Combust. Flame 39:321 (1980).

31. Miles, P.C., Ph.D. Diss., Cornell University, 1991.

32. Gouldin, F.C. and Miles, P.C., Combust. Flame, 100:202-210 (1995).

33. Castleman, K.R., Digital Image Processing, 2nd Ed. Prentice Hall, Englewood Cliffs, NJ, 1996.

34. Gülder, O.L., Proc. Combust. Inst. 23:743-750 (1990).

35. Tseng, L.-K., Ismael, M.A., and Gaeth, G.M., Combust. Flame, 95:410-426 (1993).

36. Trouve, A. and Poinsot, T., J. Fluid Mech. 278:1-31 (1994).

37. Poinsot, T., Echekki, T., and Mungal, M.G., Combust. Sci. Technol. 81:45-73 (1992).

38. Hirasawa, T., Ueda, T., and Matsuo, A., Combust. Flame 121:312-322 (2000).

39. Sinibaldi, J.O., Mueller, C.J., and Driscoll, J.F., Proc. Combust. Inst. 27:827-832 (1998).

40. Chen, J.H., Im, H.G., Proc. Combust. Inst. 27:819-826 (1998).

41. Lourenco, L, and Krothapalli, A., Exp. Fluids 18:421-428 (1995).

42. Lawson, N.J., and Wu., Meas. Sci. Technol. 8:1455-1464 (1997).

43. Gomez, A. and Rosner, D.E., Combust. Sci. Technol. 89:335 (1993).

44. Haghgooie, M.I., Theory of Jets in Ideal Flows. Academic Press, New York (1965).

45. Melling, A. Meas. Sci. Technol. 8:1406-1416.

46. Gilbert, M., David, L., and Altman, D., Jet Propulsion, 25:26-30 (1955).

47. Bergthorson, J.M., Ph.D. Diss., California Institute of Technology, (2005).

48. Sung, C.J., Law, C.K., and Axelbaum, R.L., Combust. Sci. Technol. 99:119-132 (1994).

49. White, F.M., Viscous Fluid Flow, 2nd ed. McGraw-Hill, New York (1991).

50. Talbot, L., Cheng, R.K., Schefer, R.W., et al. J. Fluid Mech. 101:737-758 (1980).

51. Allen, M.D., and Raabe, O.G. Aerosol Sci. Technol. 4:269-286 (1985).

52. Brock, J.R., Journal of Colloid Science, 17:768-780 (1962).

53. Chemkin, Release 4.1, Reaction Design (2007).

54. Cantera, Release 1.7.0, California Institute of Technology (2006).

55. Knaus, D. A., Sattler, S. S., and Gouldin, F. C., Combust. Flame, **141**:253-270 (2005).

56. Stanford Research Systems, Model DG535 Digital Delay/Pulse Generator, Revision 2.9, Sunnyvale, CA (2006).

57. Matlab version 6.1.0.450 Release 12.1, The MathWorks, Natik, MA.

58. Castleman, K.R. Digital Image Processing. Prentice Hall, Englewood Cliffs, New Jersey, 2nd ed., 1996.

59. Sattler, S. S., Knaus, D. A., and Gouldin, F. C., Proc. Comb. Inst. **29:**1785-1792 (2002).

60. van Doorne, CWH, Westerweel, J., Exp. in Fluids, 42:259-279 (2007).

61. Reungoat, D., Riviere, N., and Faure, J.P. J. of Visualization 10:99-110 (2007).

62. Watanabe, Y., Hideshima, Y., Shigematsu, T., et al, Meas. Sci. and Technol. 17:1456-1469 (2006).

63. Perret, L., Braud, P. Fourmet, C., et al, Exp. in Fluids 40:813-824 (2006).

64. Larass, N., Boukhalfa, A., Trinite, D., 10th Int. Symp. on App. of Laser Tech. to Fluid Mech. (2000).

65. Amantini, G., Frank, J.H., Smooke, MD., et al Combust. Theory and Modelling 11:47-72 (2007).

66. Amantini, G., Frank, J.H., Smooke, M.D., et al Combust. Flame 147:133-149 (2006).

67. Amantini, G., Frank, J.H., Gomez, A., Proc. Combust. Inst. 30:313-321 (2005).

68. Mansour, W.S., Exp. Thermal Fluid Sci. 28:771-779 (2004).

69. Frank, J.H., Kalt, P.A.M., Bilger, R.W. Combust. Flame 116:220-232 (1999).

70. Susset, A., Trinite, M., Honore, D., Proc. Combust. Inst. 27 (1998).

71. Honore,D., Lecordier, B., Susset, A., et al Exp. Fluids 29:S248-S254 (2000).

72. Filatyev, S.A., Driscoll, J.F., Carter, C.D., et al Combust. Flame 141:1-21 (2005).

73. Stella, A., Guj, G.L., Kompenhans, J. et al, Aerospace Sci. Technol. 5:357-364 (2001).

74. Kim, Y.M., Kim, H.J., Combust. Sci. Tech. 137:51-80 (1998).

75. Sung, C.J., Kistler, J.S., Nishioka, M., and Law, C.K. Combust. Flame 105:189-201 (1996).

76. Rosner, D.E. Transport Processes in Chemically Reacting Flow Systems. Butterworth Publishers, Stoneham, MA, 1986.

77. Sinibaldi, J.O., Driscoll, J.F., Mueller, C.J., et al, Combust. Flame 133:323-334 (2003).

78. Im., H.G., and Chen, J.H., Combust. Flame 126:1384-1392 (2001).

79. Gran, I.R., Echekki, T., and Chen, J.H., Proc. Combust. Inst., 26:323 (1996).

80. Sinibaldi, J.O., Driscoll, J.F., Mueller, C.J., et al, Combust. Flame 133:323-334 (2003).

81. Echekki, T., and Chen, J.H., Combust. Flame, 116:184 (1996).

82. Chakraborty, N., and Cant, S. Combust. Flame 137:129 (2004).

83. Jenkins, K.W., Klein, M., Chakraborty, N. et al. Combust. Flame 145:415 (2006).

84. Chakraborty, N., and Cant, R.S., Phys. Fluids 17:105 (2005).

85. Liao, et al Fuel 83:1247-1250 (2004).

86. Mungal, M.G., Lourenco, L.M., Krothapalli, A., Combust. Sci. Tech. 106:239-265 (1995).

87. Bevington, P.R., Data Reduction and Error Analysis for the Physical Sciences, New York:McGraw-Hill (1969).

88. R statistical computing website: www.r-project.org February 2008.